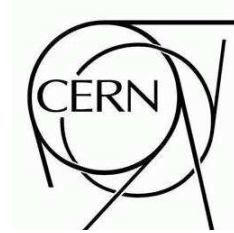




# ATLAS NOTE

ATL-ATL-INDET-PUB-2007-xxx, V2.2

August 13, 2007



## Pixel Offline Analysis for EndcapA Cosmic Data

The ATLAS Pixel Group

### Abstract

This document summarizes the results of the offline analysis for the pixel endcapA system test cosmic data. The setup consists of one pixel endcap of three disks, for a total of 144 modules and 6.6 million channels, about the 8% of the full detector with the goal of exercising the readout system, data taking and testing the offline reconstruction chain. The observed noise occupancy per readout (BCID) is found to be  $10^{-10}$  after removing all the noisy pixels. Comparison with the detector characterization performed during the detector assembly shows that most of these noisy pixels were already flagged during the production test. The tracking studies, especially the ones related to particles passing in the overlap regions between adjacent modules, have been very useful in spotting problems in our geometry description and can be used for the relative alignment between the adjacent modules. The characteristic of pixel clustering in the data are checked and agree well with Monte Carlo simulation. The pixel cluster efficiency are also measured to be close to 100% using the hits in the module overlap regions. When using the geometry taken from the detector survey, an initial resolution of  $21.2 \mu m$  is obtained. After a preliminary alignment this improves to  $17.8 \mu m$ . The difference with the  $15.8 \mu m$  expected from MC simulation are probably due to residual alignment uncertainties which are under investigation.

# 1 Introduction

In December 2006 an endcap of the ATLAS pixel detector was used to perform a commissioning test of the detector. For the first time production part of the pixel detector consisting of 144 modules, out of a total number of 1744, was completely equipped with services and managed by a initial production of the ATLAS DAQ system components.

The Endcap has been operated in an environmental chamber withing the clean room used for the ATLAS Inner Detector assembly in the CERN SR1 building.

These operation has been an important step in the commissioning of the detector, showing that the full services, the communication chain between the on-detector and the off-detector electronics, the DAQ and DCS hardware and software systems are properly integrated and capable to drive the detector.

The description of the components of the pixel detector and the readout electronics and Detector Control System will be described in detail in a Pixel Detector paper under preparation [1].

A lot of experience has been gained in SR1 running and is applied to the assembly of the final services. The results from the analysis of the performance of services are the subject of an accompanying ATLAS note [2]. That note will also contain the tests performed in order to calibrate the whole detector and prepare it for the data taking.

This note describes the results of the running of the system and the analysis of the data collected by the detector in two running modes:

1. with random triggers, in order to measure noise occupancy;
2. using a scintillator system to trigger on cosmic rays.

Noise measurements with random trigger have been taken in different conditions and are used to derive a number of useful information for understanding detector properties and tuning the simulation:

1. the amount of *fixed pattern noise*, i.e. channels with higher than normal occupancy, and the correlation between these channels and the one detected as *special* during the module acceptance tests;
2. the rate of random noise. Previous test beam operation could only put an upper limit on the level or random noise [3].
3. Time over Threshold (TOT) spectrum for noise: differently from naïve expectation, this has proven not to have a Gaussian distribution and a more complex model needs to be setup for that;
4. dependence of noise rate from operational conditions: trigger rate, depletion voltage, threshold settings.

Running with cosmic rays is used to derive information that needs a physics signal. Unfortunately the time devoted to cosmic runs was not enough to collect the statistics needed to check functionality of every single channel, but the amount of data written on disk is useful for:

1. checking the overall resolution and tracking reconstruction;
2. validating the simulation by comparing cluster size, ToT spectrum and timing distribution with what can be observed on the data and the calibration information;
3. exercising the alignment algorithms using tracks passing through overlapping regions between modules.

This effort is also the base for the next commissioning run with cosmics in the pit.

The note is organized as follows: at first a description of the setup geometry and cosmics trigger is given, then will be reviewed the results obtained with noise runs. After that the modification to the ATLAS tracking to reconstruct cosmics tracks will be described. In this section also overall tracking efficiency and rate will be computed, in addition to Monte Carlo validation using cosmics clusters and, finally, results on alignment and resolution.

## 2 Pixel EndCap A Cosmic Muon Setup

The pixel endcap A cosmic muon test [4] is using the same setup as the pixel system test in the SR1 building at CERN [5]. The cosmic test is a logical continuation of the system test with the goal of exercising the readout system, data taking and testing the offline reconstruction chain.

The aim is to collect a larger cosmic muon sample to reconstruct tracks passing through the detector, study their properties and perform a simple alignment of the detector using overlap regions on the pixel disks.

### 2.1 Pixel EndCap A Geometry

The pixel endcap A is one of the two end sections of the pixel inner detector, its geometry is described in [7]. It consists of three disks placed at 49.5 cm, 58.0 cm and 65.0 cm in the  $z$ -direction. There are 48 modules on each disk, i.e. 144 modules in the entire pixel endcap A. Each disk has 24 modules on the even (odd) side respectively. The even side is closer to the interaction point. The modules centers (i.e. the middle of the silicon wafer) are displaced by 4.276 mm according to the survey (the thickness of the disk implemented in the reconstruction software is only 4.2 mm however, the discrepancy will be discussed further in this note). The first module is positioned at  $3.75^\circ$  in  $\phi$ , every other modules is rotated by  $7.5^\circ$  in  $r\phi$  plane with respect to the previous module. The centers of modules are placed at 119.17 mm in radius.

The module consists of 16 front-end chips bump bonded to the silicon wafer (average thickness of  $256\mu\text{m}$ , the area  $(x,y) = 1.88\text{ cm} \times 6.3\text{ cm}$ , that includes all guard rings), there are two rows of eight FE chips on each module. The active area of the sensor is  $(x,y) = 1.64\text{ cm} \times 6.08\text{ cm}$ , each front end chip covers  $0.76\text{ cm} \times 0.82\text{ cm}$ , it has 16 columns of  $400\mu\text{m}$  and 2 columns of  $600\mu\text{m}$  (so-called *long*) pixels, and 160 normal plus 4 *ganged* rows of  $50\mu\text{m}$  pixels. The geometry of the module and its dimensions are well described in [8]. This is why the short side (local X direction) of the module has a  $50\mu\text{m}$  pitch and the long side (local Y direction) has a  $400\mu\text{m}$  pitch with the only exception of ganged pixels. They are cross connected and receive a special treatment in the simulation/reconstruction code. The position of a module on a disk is defined by the module  $\eta$  index (it is the same for the even and odd side modules of a particular layer, it is 0, 1 and 2 for disk 1A, disk 2A and disk 3A respectively) and the module  $\phi$  (it goes from 0 to 47, and we use it to distinguish front (=even), back(=odd) modules on one disk). The module  $\phi$  id can be used to calculate the  $\phi$  of the module center by using Eq. 1.

$$\phi_c = (\phi_{mod} + 0.5) \times 7.5 \times \pi / 180 \quad (1)$$

The properties, position and status (ON=in readout, OFF=out of readout) of pixel endcap A modules is given in Figs. 1, 2, 3, 4, 5 and 6.

The  $(x,y)$  position of a pixel on pixel endcap module is defined by the  $\eta$  index (local Y-axis,  $\eta$  direction, column number) and  $\phi$  index (local X-axis,  $\phi$  direction, row number). There are 144 columns (coarse pitch) and 328 rows (fine pitch) on the module. The  $\eta$ ,  $\phi$  index numbering is described in Fig. 7. The  $\eta$  index increases with an increasing radius, i.e. decreasing  $\eta$ , and the  $\phi$  index increases with increasing global  $\phi$ , i.e. it is counted in the opposite direction for the even and odd side modules. The

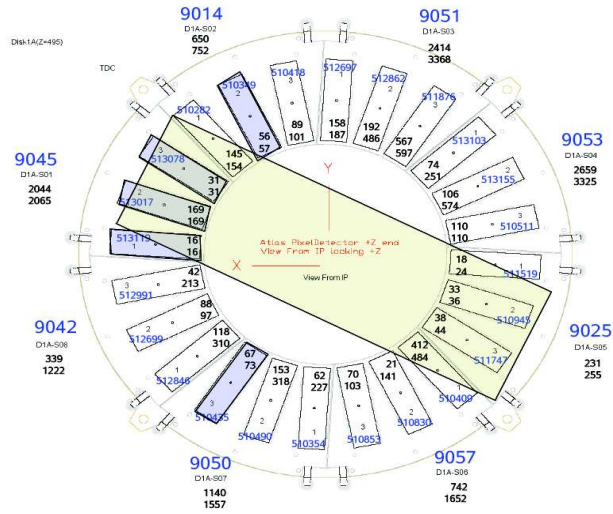


Figure 1: Disk 1A even side modules.

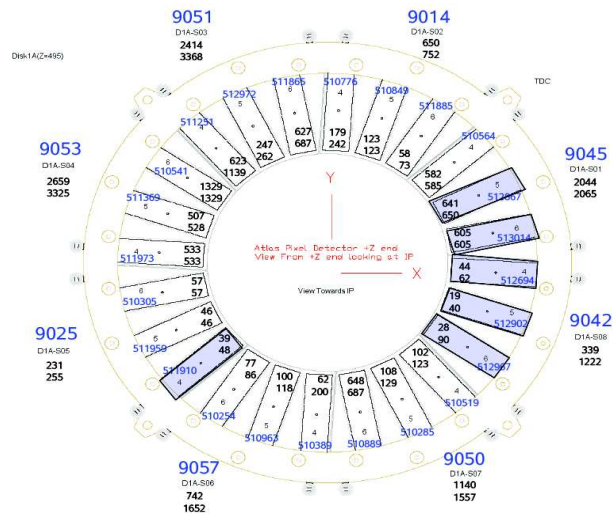


Figure 2: Disk 1A odd side modules.



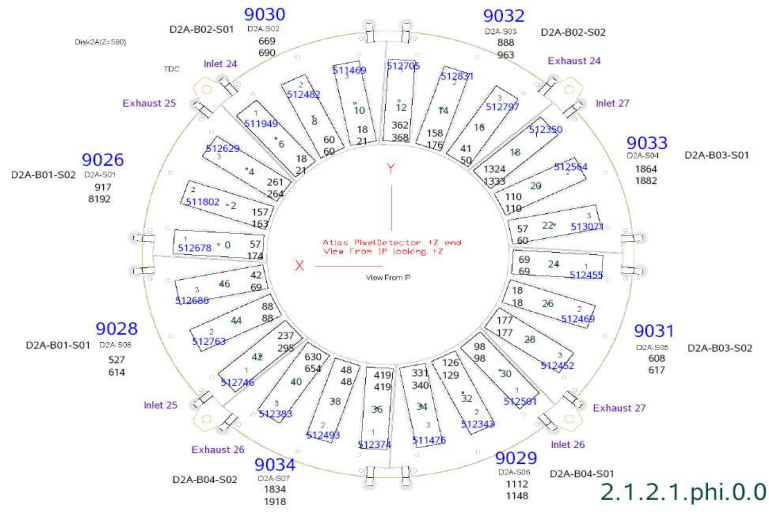


Figure 3: Disk 2A even side modules.

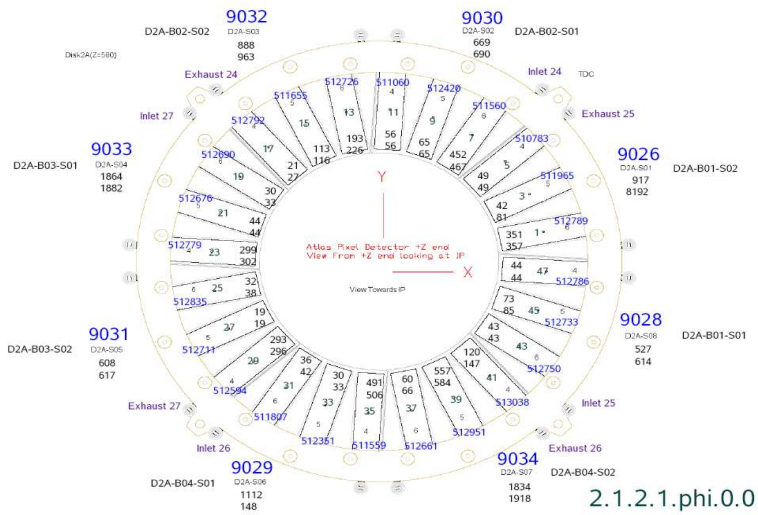


Figure 4: Disk 2A odd side modules.

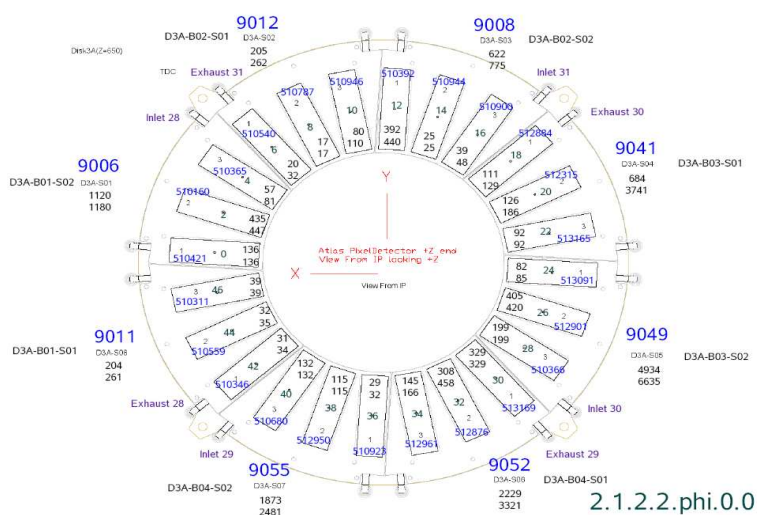


Figure 5: Disk 3A even side modules.

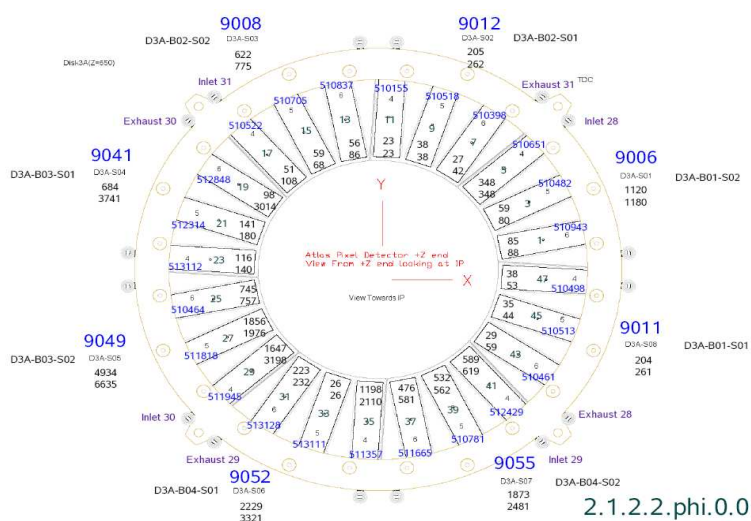
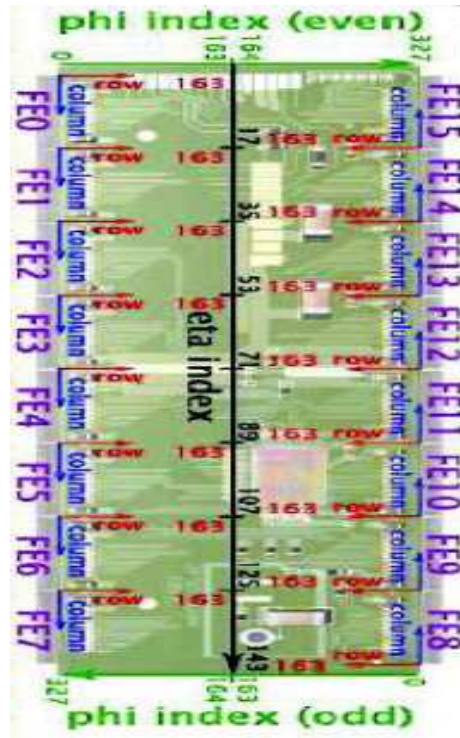


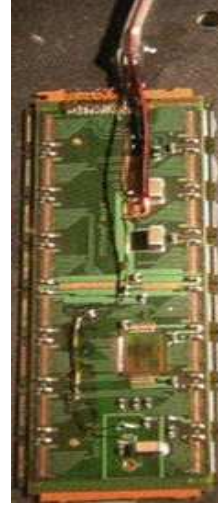
Figure 6: Disk 3A odd side modules.

same rule is also applied for the local coordinate system on the pixel endcap module with the coordinate center defined as a center of the module (that is the actual center of the silicon sensor). Note that the even module local X coordinate orientation is the same as the local X of an odd module.



### Type-0 cable side

**Higher radius  
i.e. lower  $\eta$**



**Lower radius  
i.e. lower  $\eta$**

Figure 7: Definition of row and column indices on the pixel endcap module.

The global coordinate system is defined in Figs. 1, 2, 3, 4, 5 and 6.

## 2.2 Cosmic Setup

The pixel endcap A cosmic setup consists of the pixel endcap A that is hooked up inside the dry box providing the required environment for the pixel endcap operation (dry air mainly), a prototype service quarter panel (PSQP) connected to all outside services (cooling, low voltage and high voltage distribution and regulation, readout, environmental information etc.). Both the pixel endcap and PSQP are placed inside the dry box. The endcap hangs vertically inside the dry box (i.e. its axis is perpendicular to the table top), that is an obvious requirement to maximize the flux of cosmic muons passing through the pixel endcap fiducial volume as well as to maximize the number of at least 3-hit tracks.

### 2.2.1 Mechanical design

The trigger system [9] (dimensions of the system are given in Fig. 8) consists of four SLAC scintillators, two smaller scintillators are placed above each other (the top scintillator only 21 cm above the end section, i.e. 23.5 cm above disk 3A or 39 cm above disk 1A and the bottom scintillator 120.0 cm below the top one, i.e. 96 cm below the disk 3A). The small scintillators (45.8 cm  $\times$  71.2 cm) are centered

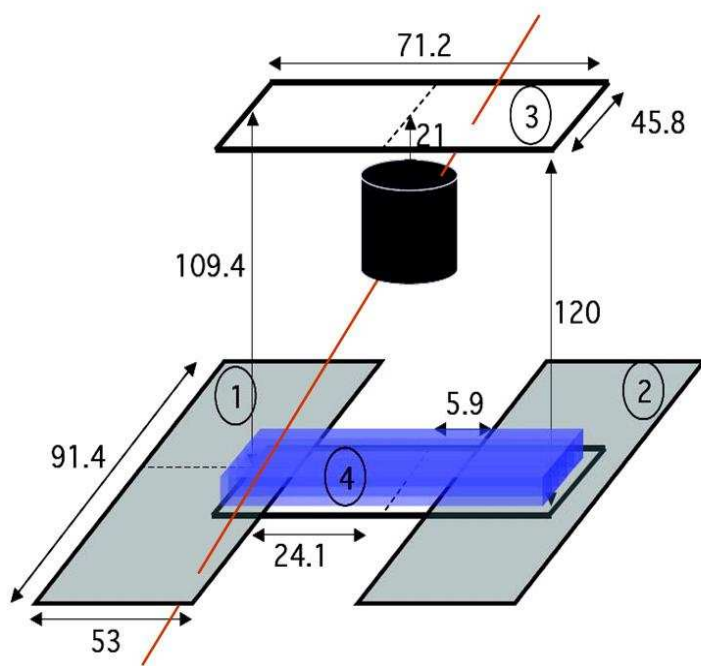


Figure 8: Schematics of a pixel endcap A cosmics setup.

around the z-axis of the end section. The top scintillator is referred to as scintillator no. 3 and the bottom one as scintillator no. 4. These two scintillators are the bare minimum to have a good coincidence circuit (described in Fig. 12), the top scintillator is required to trigger the cosmic muon and the bottom scintillator defines geometrically the acceptance of the trigger system. There are many muons that leave the signal in scintillators 3 and 4 but never pass through the pixel endcap or leave only one/two hits. The endcap A is rotated by  $-\pi/8$  with respect to the y-axis of the dry box (the y-axis of the dry box is parallel to the long side of the dry box table, i.e. axis of the PSQP). This rotation can be seen in Fig. 1.

Additionally, we had a luxury of additional two large scintillators that improve the trigger efficiency of the system. The ideal placement of large scintillators (referred to as scintillator 1 and 2) would be on the sides of the dry box so that they can cover even large incidence angles, see Fig. 9 for such an ideal topology. This placement however turned out to be very difficult to implement because of the access to the pixel endcap during the system test operation. At the end, we have decided to place large scintillators under the table top of the dry box. The dimensions of large scintillators are 53.0 cm  $\times$  91.4 cm.

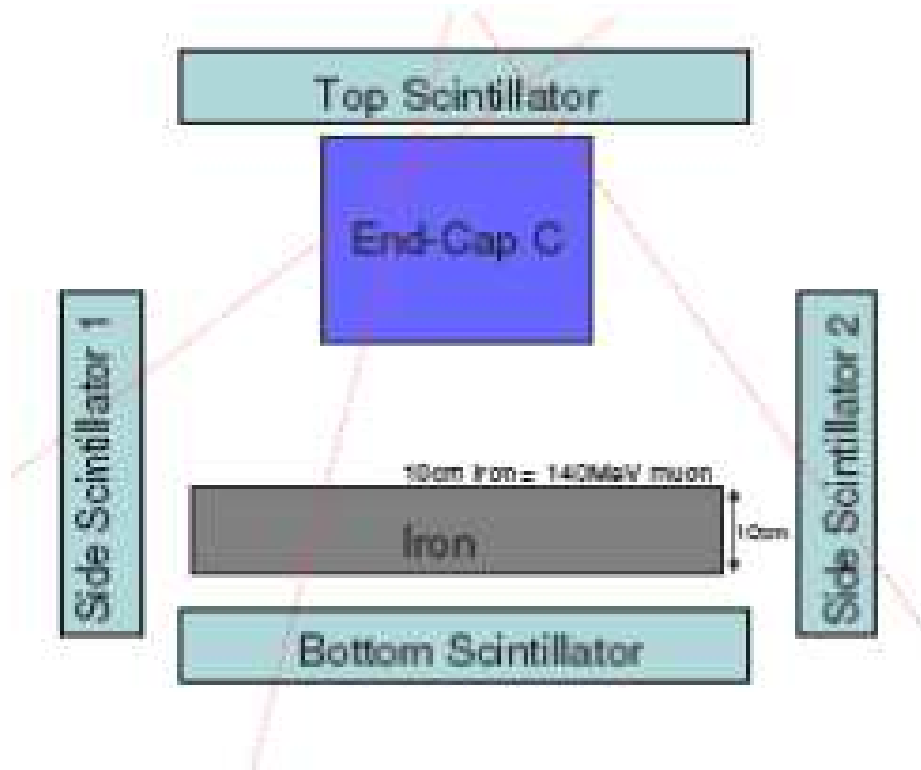


Figure 9: Schematics of an ideal pixel endcap A cosmic trigger system setup.

Whereas the placement of top and bottom small scintillator is naturally determined by the length (or height in this particular case) of the endcap, the height of the PSQP and by the access essentially required to connect exhaust copper extension tubes to the endcap cooling pipes, in order to decide what is the optimal placement of large scintillators, we had to run a toy Monte Carlo simulation to make a decision. The results of this simulation are presented in Fig. 10.

The aim of this study was to maximize the weighted hit density coverage on the surface of the bottom

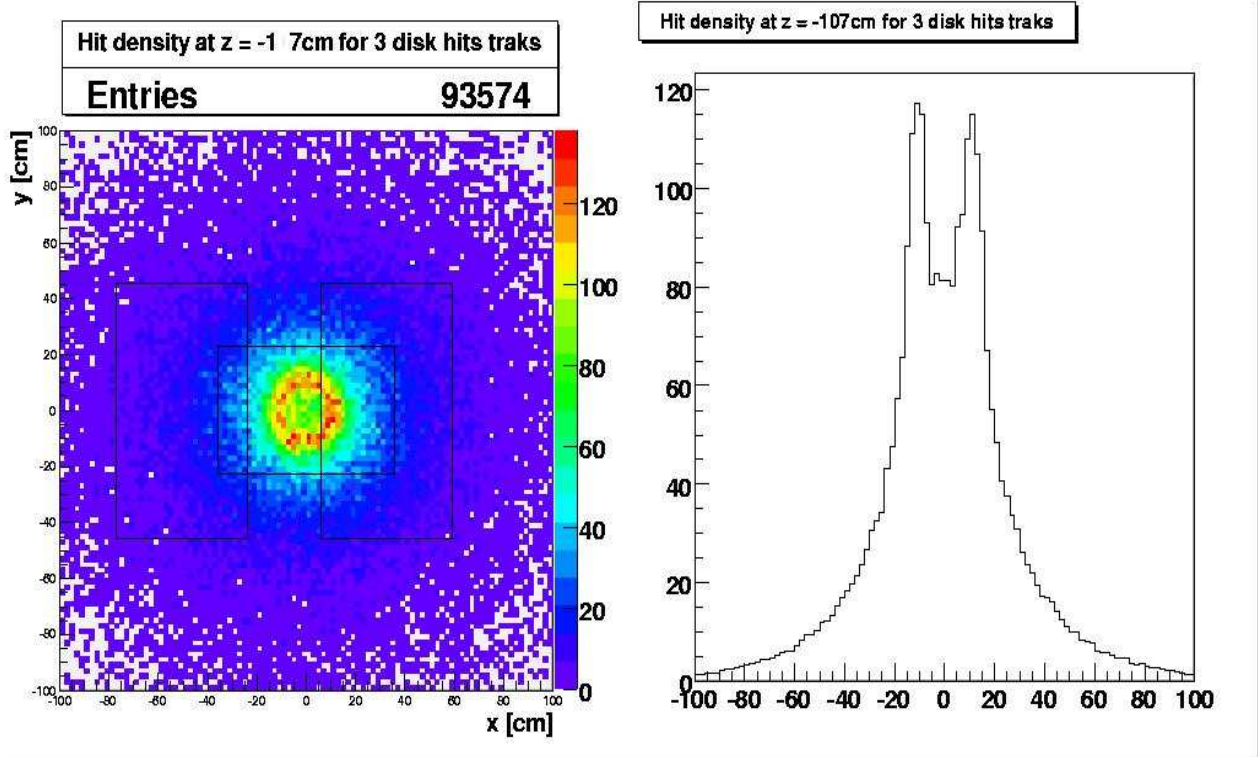


Figure 10: Toy Monte Carlo study dedicated to optimize the large scintillator placement.

large scintillators (left plot in Fig. 10). At the same time, there are further restrictions for the placement of bottom large scintillators, such as: (a) they cannot be possibly centered around the axis of the pixel endcap because of legs of tables holding the endcap dry box, (b) the bottom small scintillator itself that is only 11.5 cm above the large scintillators, (c) the mounting brackets of the frame of large scintillators. The ideal placement (see Fig. 11) is perpendicular to the small scintillators only 11.5 cm above the bottom scintillator. Due to the reason outlined above, there is a placement offset along the y-direction (i.e. long side of the table, small scintillators), which is 24.1 cm with respect to the pixel endcap z-axis (and the center of small scintillators) for scintillator no. 1 and 5.9 cm in the opposite direction for scintillator no. 2.

To remove low momentum cosmic muons which suffer most from the multiple scattering, we have also investigated the possibility to filter them out by an extra layer of iron between scintillators 3 and 4, directly below the endcap. Due to the support of PSQP, we had a possibility to break the iron layer into two parts: one above the endcap and the other below the PP0 panel of the PSQP. The maximal thickness that we could place on the table would be less than 300 kg. We could not put there more because more than  $\sim 750$  kg would compromise the safety of the device due to the extra weight concentrated on the building floor and the table itself. Another constraint was very little space under the PSQP. There was something like 15 cm of space between the rails that hold the PSQP, we could not use more than  $\sim 12$  cm because the iron had to be inserted manually and we had to be very cautious about damaging the PSQP. Finally, only  $\sim 12$  cm of iron in the forward region of the setup was compromised. That is an equivalent to saying that we are cutting out all muons under 140 MeV. In order to reduce the multiple scattering significantly we would need at least  $\sim 500$  MeV cutoff.



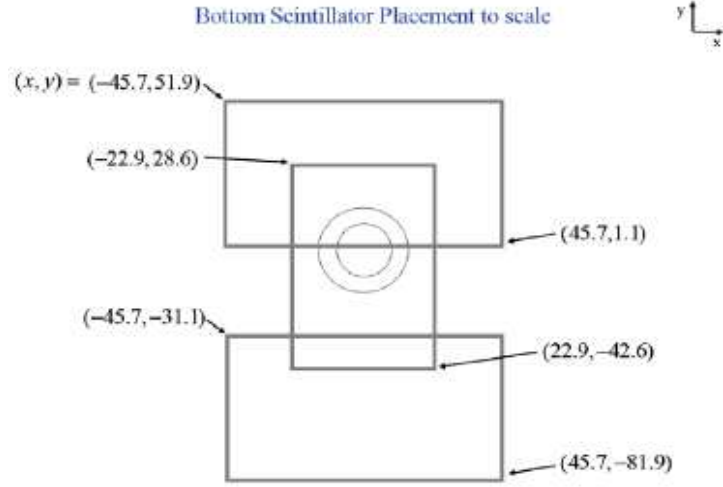


Figure 11: Placement of large scintillators, view from the top, towards interaction point.

### 2.2.2 Coincidence circuit

The layout of a coincidence circuit is given in Fig. 12. The starting point is to require a signal in the top scintillator (scintillator no. 3) and require logical *AND* with logically *OR* of all bottom scintillators (one of them is the small bottom scintillator, and two are the large ones in the front and back of the setup).

In the cosmic trigger and readout system we had three crates (the following describes an ideal signal path):

- *NIM crate*: it was a crate with all the HV power supplies for the PMT tubes in the setup and the logic electronics (discriminators, delay units and AND/OR units). The main idea was to keep the discriminators close to the setup so that we avoid any attenuation over the long distances and only transfer the TTL signal from the discriminators over more than 50 m long cables. This crate was about 2 meters away from the setup, inside the clean room of the SR1 building. The final output of the AND logical unit comes out of the crate as an input for TDC in the VME crate in the rack area, it is actually equivalent to L1A Trigger accept in the real experiment.
- *VME crate*: this is a crate that holds SBCs, LTP, TTC and a BUSY unit (OR). The TDC receive TTL signal from discriminators and AND/OR logic unit, and in principal we could use this information for some timing study. However, we never got a chance to do it and this information is not available offline. This is why only the output of the AND/OR unit is received by LTP, transferred to TTC and finally to TIM in the ROD/DAQ crate.
- *DAQ crate*: it consists of several RODs (12 RODs needed to readout all 144 modules in endcap A) and TIM. The trigger signal from TTC (in VME crate) goes to TIM and then gets distributed among RODs. In the reality we had 2 DAQ crates, one with 8 RODs and the other with 4 RODs.

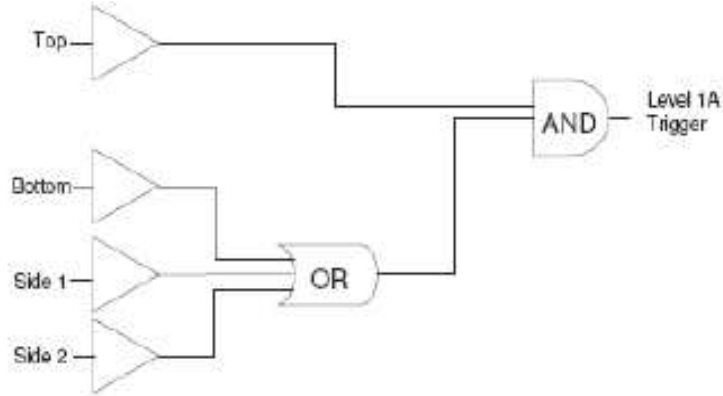


Figure 12: Coincidence circuit.

### 2.2.3 Cosmic muon rate

The expected cosmic muon rate was studied extensively using the toy Monte Carlo simulation, full ATLAS Pixel Detector simulation and cross-checked with the back of the envelope calculations.

The integral intensity of vertical muons above 1 GeV/c at sea level is  $70 \text{ m}^{-2}\text{s}^{-1}\text{sr}^{-1}$  [10]. It is an equivalent of 1 cosmic muon per  $\text{cm}^2$  every second. The distribution of cosmic muons is roughly  $\cos^2\theta$  of the incidence angle, it is symmetric in  $\phi$ , the mean of the cosmic muon momentum on the sea level is  $\sim 4 \text{ GeV}/c$ .

The toy Monte Carlo start with a randomly distributed cosmic muon passing through the top level scintillator, it assumes the  $\cos^2\theta$  incidence angle distribution, and a full symmetry in the  $\phi$  angle. It has a flat momentum distribution. No detector effects are assumed, this is why this assumption is sufficient to estimate the cosmic muon rate. The overall trigger efficiency is expected to be close to 85 % and the disk hit efficiency is roughly 90 %. We count how many times the cosmic muon will pass through the bottom scintillator(s) and how many hits will be associated to a muon traversing the fiducial volume of the endcap given the geometry of the detector.

The full ATLAS pixel detector simulation takes all the detector effects into account. We start with the cosmic muon generated in cosmic muon generator (it has all angular and momentum distributions simulated correctly), count how many times do we have a coincidence in the top and bottom scintillators, simulate the response of the detector to cosmic muon passing through the sensitive layers, build space points/hits and reconstruct tracks. We also count the number of tracks and hits on the tracks to estimate the trigger rate and the track reconstruction efficiency (convoluted with the detector acceptance indeed).

The toy Monte Carlo estimates the cosmic muon rate through the top scintillator is 54 Hz and the trigger rate with all four scintillators is 16 Hz. The full detector simulation gives 6 Hz for the coincidence of top and bottom scintillator and 18 Hz for all four scintillators. These two values are in a good agree-



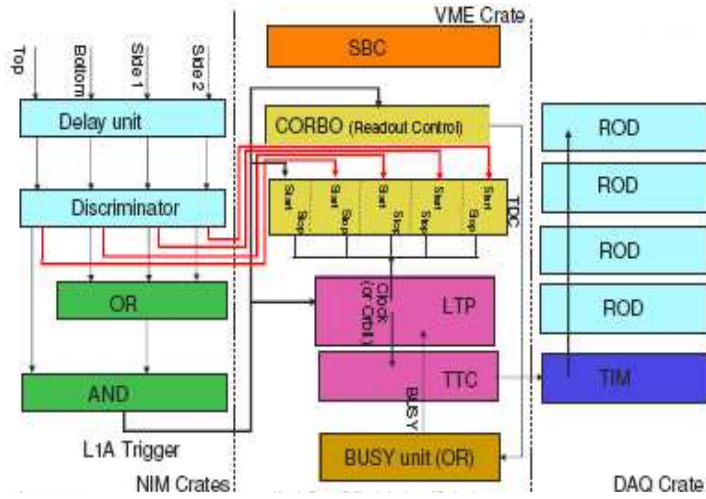


Figure 13: Ideal signal path.

ment with the trigger rate measured in the DAQ system, we have recorded cosmic data with a data taking frequency of about 15 Hz.

The track reconstruction efficiency (again, convoluted with the detector and setup acceptance), if all 144 modules are readout, estimated from the simulated data was expected to be in the vicinity of 6 %, i.e. we would expect roughly one three hit cosmic muon track every second. In the reality, only 115 modules were readout, some disabled modules have clustered in space (e.g. the whole sector, i.e. 6 modules, were disabled) and that is why the track reconstruction should be 20-30% lower than that, i.e.  $\sim 4\%$ . This is really what we have measured in the data,  $\varepsilon = 3.8\%$  (see following sections of this note). The ideal cosmic muon rate for at least 3-hit tracks is 1.5 Hz, and probably about 1 Hz for the detector with 29 disabled modules.

The track properties are affected by our choice of the cosmic trigger system layout. For example, the fact that the small scintillators are rectangular will deform the initial flat angular  $\varphi$  distribution into a sin wave distribution. The fact that the scintillators are rotated with respect to the end section by  $\pi/8$  will shift the  $\varphi$  angular distribution by this amount to the negative side. Another interesting feature is that modules missing in the readout will create dips in the angular  $\varphi$  distribution (see the following section of this note for details). There were many reasons for having that many modules disabled from the readout: disconnected cooling loop, malfunctioning opto board, missing bias voltage, missing NTC reading, etc. All these effects were also implemented in the detector simulation, see Fig. 14.

## 2.3 Cosmic setup simulation

The goal of the simulation chain is to preserve existing ATHENA structure and geometry of packages as much as possible without introducing too many changes. The reason is that one of the cosmic test priorities is to validate the simulation/reconstruction chain from the beginning to the end, i.e. from simulation, digitization, bytestream converter all the way to reconstructed tracks and alignment. This is why if we find any abnormalities, bugs or mistakes, we would like to correct them, and make them part of ATHENA release 13. We have quite successfully managed all that with the only exception of using the combined test beam standalone tracking code with no magnetic field, that is not part of the official

release 13.

The full ATLAS cosmic setup simulation is done in the following five steps:

- *cosmic muon generator*: cosmic muons get randomly generated according to all distributions described in [10] in *CosmicGenerator* package [11]. The core of the package is an old Fortran cosmic muon generator inherited from previous experiments that is wrapped up inside the C++ code to provide the necessary interface with other ATHENA simulation packages.
- *pixel endcap A geometry*: the pixel endcap A geometry is identical to the one implemented in *PixelGeoModel* [12]. The only difference is that one has to switch off endcap C, the barrel of the pixel detector, pixel support tube, frame and services. The whole pixel detector is essentially reduced to endcap A only.
- *GEANT 4 detector simulation*: the GEANT 4 (G4) is described mainly in *G4AtlasApps* package [13]. It contains definition of all setup positions and dimensions (pixel endcap position, scintillator and iron positions/dimensions etc.). The pixel endcap A (or the pixel detector that is reduced to pixel endcap A) is positioned in its nominal position.
- *trigger system simulation*: the scintillators are placed in the right position in *G4AtlasApps*, when the cosmic muon passes through their fiducial volume, the energy is deposited in that volume and if it is above some minimum amount it is considered to be a hit in the scintillator system. The logic coincidence between two scintillators is implemented in *InDetCosmicSimAlgs* package [14]. Events where there is no coincidence between top and logical OR of bottom scintillators are skipped, only triggerable events are passed further to digitization.
- *digitization*: the digitization code is the same as it is currently implemented in release 13, the only difference is that one has to make sure that hits from modules that are not present in readout (that includes pixel endcap C and barrel modules) are not being digitized. That would cause runtime errors.

The whole simulated pixel endcap A cosmic setup can be seen in Fig. 14 bottom, and 15. The how to run the simulation code instructions are described in [16].

### 3 Study of Noise Data

For the study of the noise in endcap A several runs were performed with various trigger signals that initiated by either a cosmic trigger or an external clock(random trigger). The data from several of these runs was analysed for characteristics of the noise signal. Maps of the hits on each module were used to study the correlation between the positions of noise hits in the data and the positions of pixels that had been marked as special during the production tests of the individual modules. Figure 16 shows a comparison of the noise levels for the modules of endcap A determined from threshold scans during the production and system tests. One can see that while the noise level in the system test is slightly higher than in the production test the results generally agree well with each other.

#### 3.1 Results from Run 1125 with Cosmic Trigger

The noise occupancy in Run 1125 was computed for pixels associated to different L1-triggers, or bunch crossing id's (*BCID*), where  $BCID = 5$  corresponds to the cosmic muon signal. The *module* occupancy is defined as the fraction of pixels per module, event, and *BCID* read out, and it was computed for each of

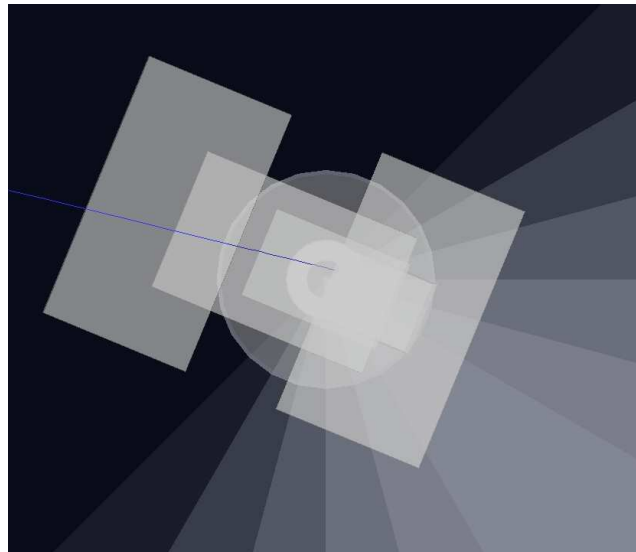
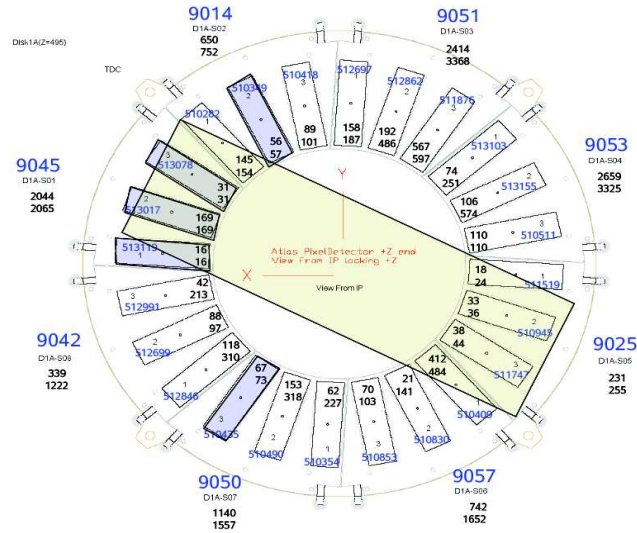


Figure 14: Simulation of the pixel endcap A cosmic setup, comparison to disk 1A, front side with small scintillator orientation. The scintillator is not up to scale.

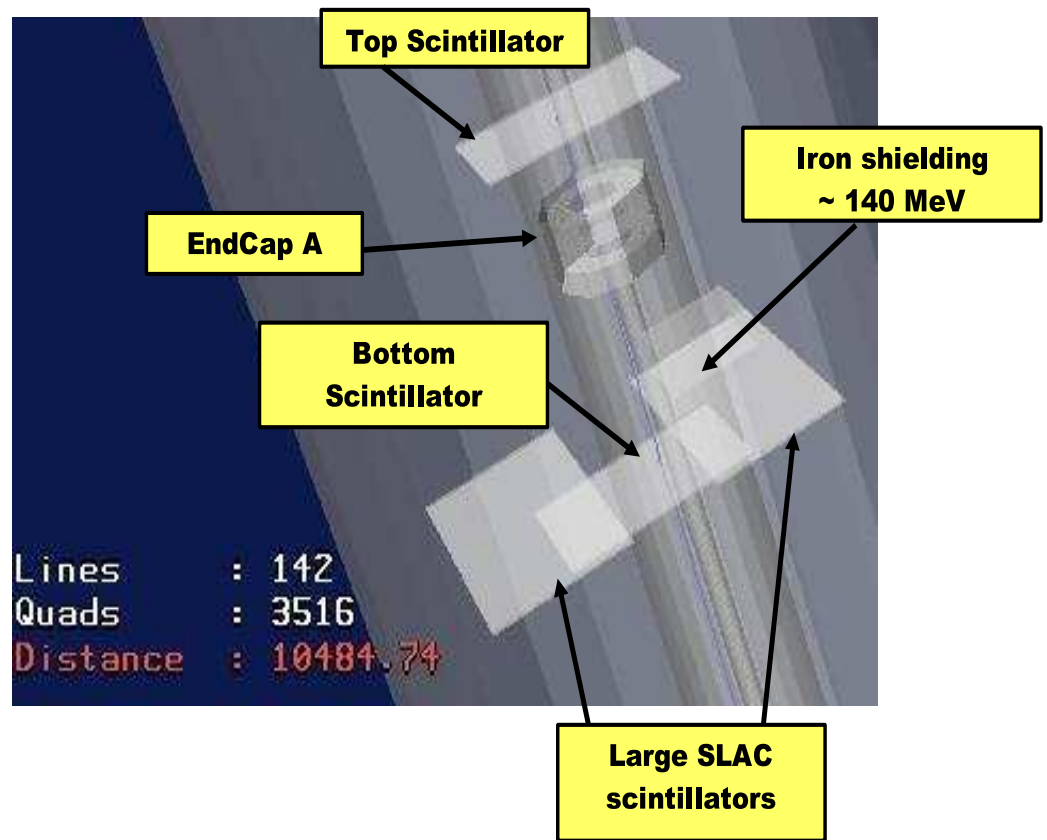


Figure 15: Simulated pixel endcap A cosmic test setup with a cosmic muon passing through it.

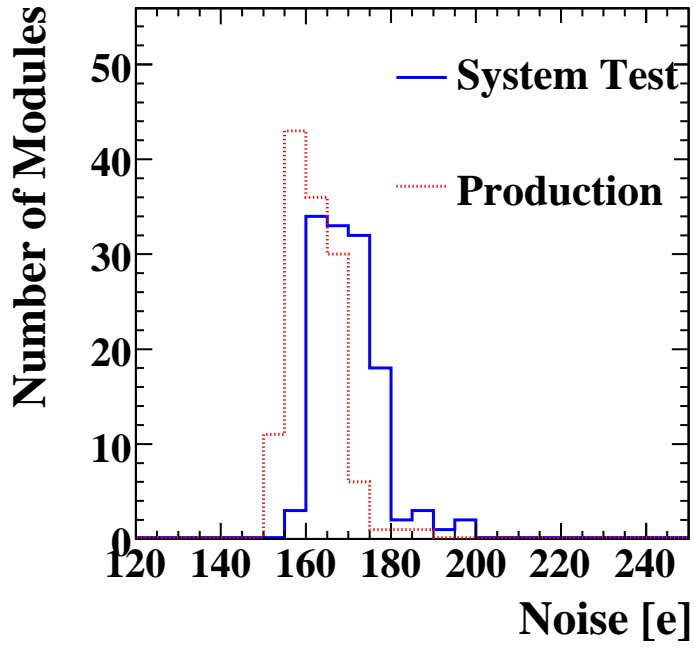


Figure 16: Noise in electrons for the modules of endcap A as determined from threshold scans during the production and system tests

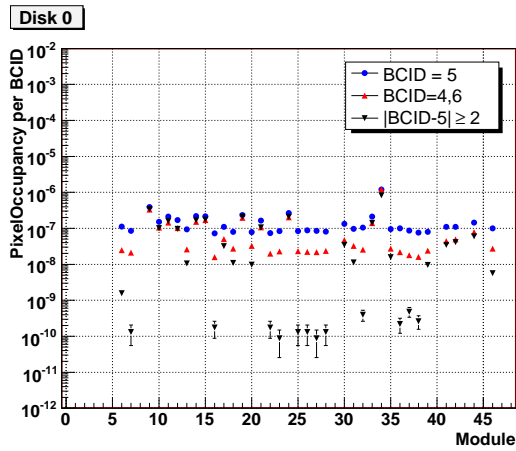


Figure 17: Module occupancies in layer 0 of endcap A during run 1125, for different L1-triggers.

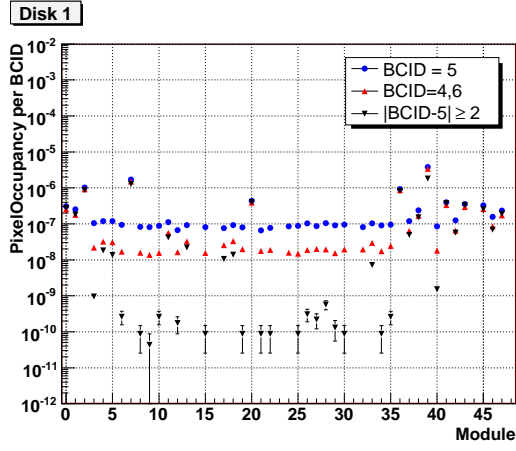


Figure 18: Module occupancies in layer 1 of endcap A during run 1125, for different L1-triggers.

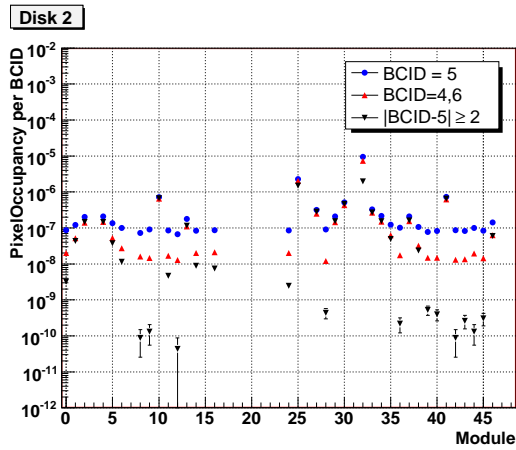


Figure 19: Module occupancies in layer 2 of endcap A during run 1125, for different L1-triggers.

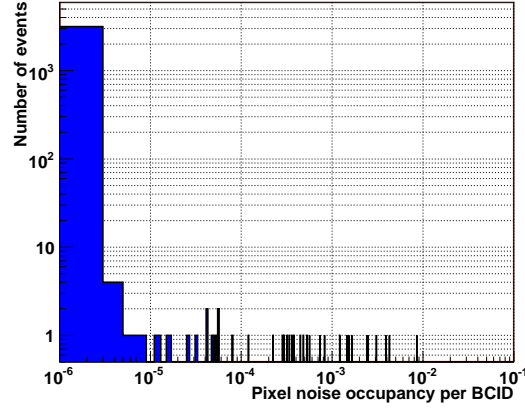


Figure 20: Pixel occupancy for low occupancy modules in endcap A layer 0.

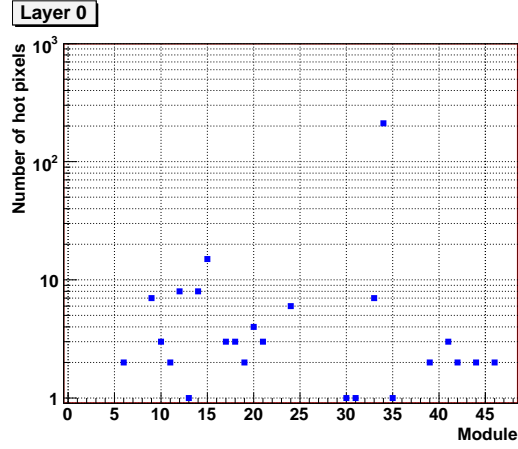


Figure 21: Distribution of hot pixels in endcap A layer 0.

the three endcap A layers, as shown in Figures 17, 18, and 19. There are large fluctuations in occupancy, in particular for events not trigger by the cosmic muons, due to the presence of hot (noisy) pixels.

The pixel occupancy, defined as the number of hits in a given pixel divided by the number of events, for several modules in layer 0 with low occupancy is shown in Figure 20.

Based on Figure 20, pixels having an occupancy greater than  $10^{-5}$  were defined as *hot* pixels. With this criteria, 1544 pixels were masked as hot pixels. Figures 21, 22, and 23 show the distribution of hot pixels for each module of the three endcap A layers.

The *BCID* of all selected (good) and hot pixels is shown in Figures 24, and 25. As expected, hot pixels generated by noise are not correlated with any L1-trigger, whereas all signal pixels cluster around the cosmic peak corresponding to *BCID* = 5.

The topology of the hot pixels within a module was investigated by looking at the distance (in units of row and column) between a hot pixel, and the closest and second closest hot pixel, as shown in Figures 26, and 27. The significant peaks at 1 indicate the presence of small *clusters* of nearby noisy pixels.

An example of such cluster of hot pixels in module 34 of layer 2 can be seen in Figure 28.

After removing all hot pixels in this run, the pixel module occupancy becomes very uniform within modules of a same layer, as it can be seen from Figures 29, 30, and 31. The pixel noise occupancy per module is of the order of  $10^{-10}$ .

The distribution of number of pixels per event before and after hot pixel removal is shown in Figures 32, 33, and 34. On average, there were 24 pixels read out per event, of which 23 were hot pixels.

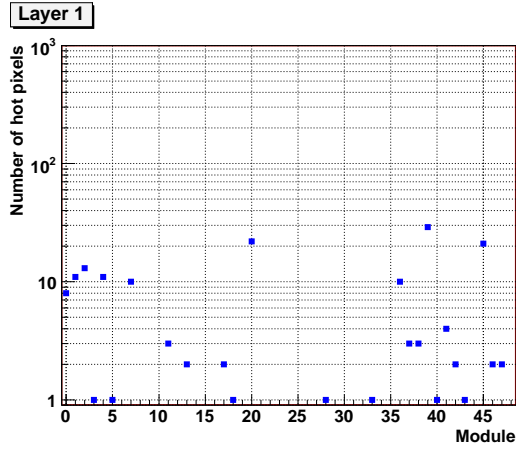


Figure 22: Distribution of hot pixels in endcap A layer 1.

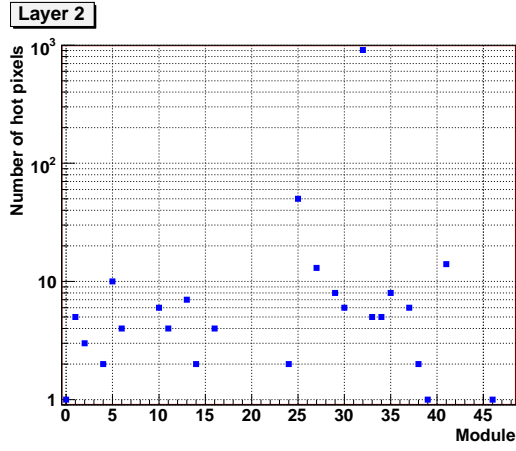


Figure 23: Distribution of hot pixels in endcap A layer 2.

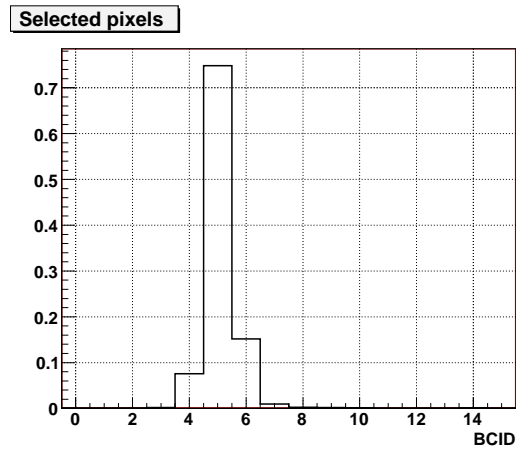


Figure 24: Bunch Crossing ID for all selected pixels not masked as hot.



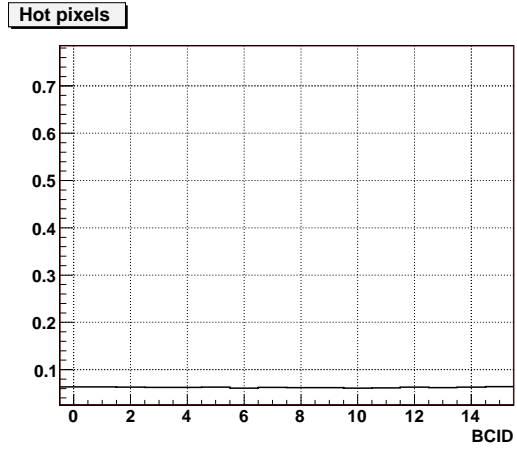


Figure 25: Bunch Crossing ID for hot pixels.

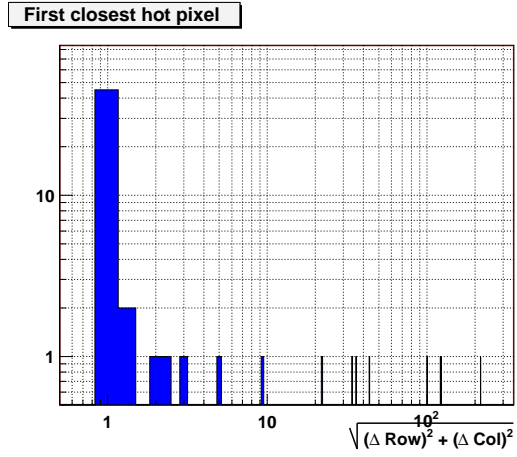


Figure 26: Distance between a hot pixel and the closest hot pixel within a module.

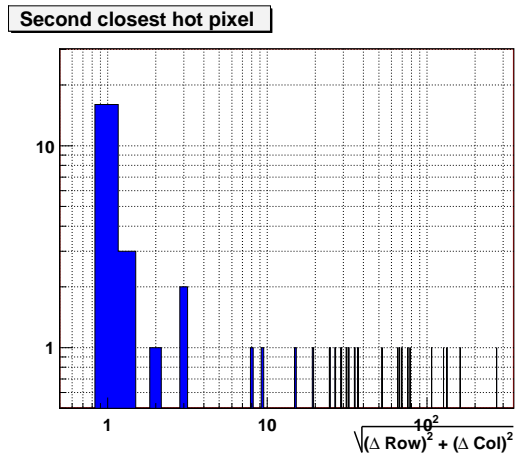


Figure 27: Distance between a hot pixel and the second closest hot pixel within a module.

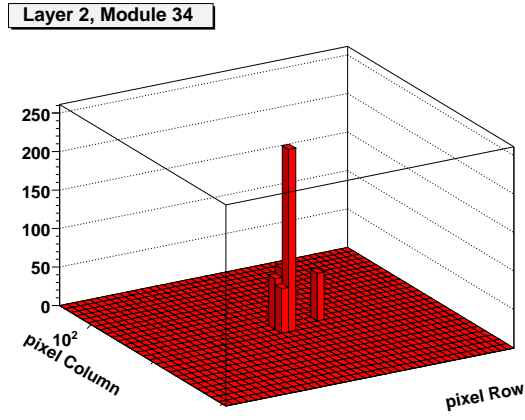


Figure 28: Example of a cluster of hot pixels in module 34 of endcap A layer 2.

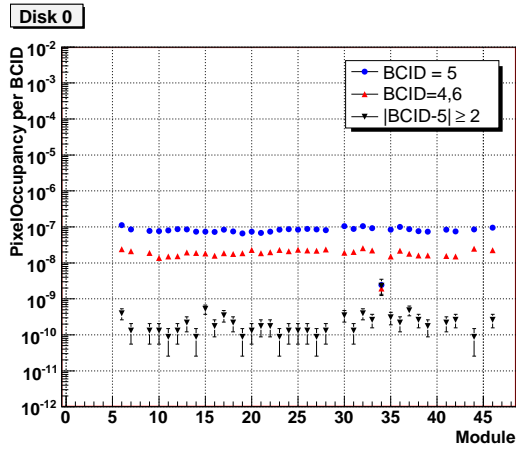


Figure 29: Module occupancies in layer 0 of endcap A during run 1125, for different L1-triggers and after hot pixel removal.

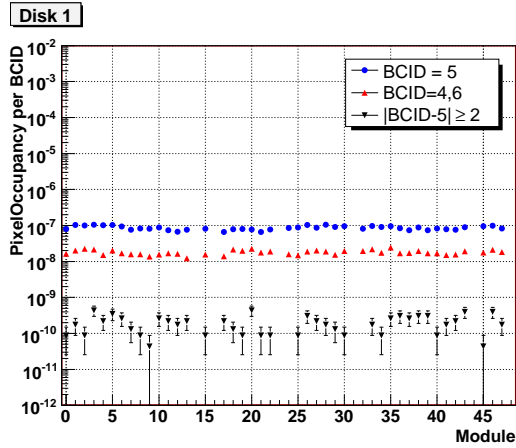


Figure 30: Module occupancies in layer 1 of endcap A during run 1125, for different L1-triggers and after hot pixel removal.

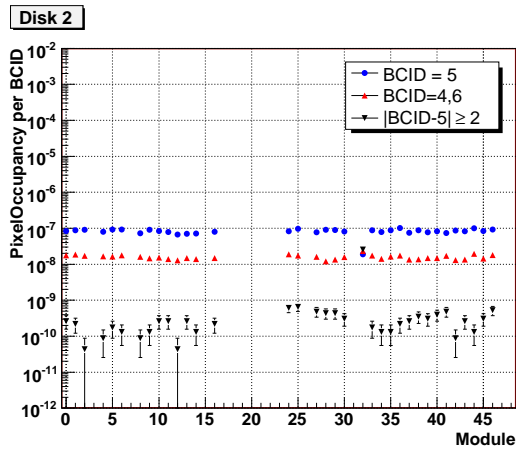


Figure 31: Module occupancies in layer 2 of endcap A during run 1125, for different L1-triggers and after hot pixel removal.

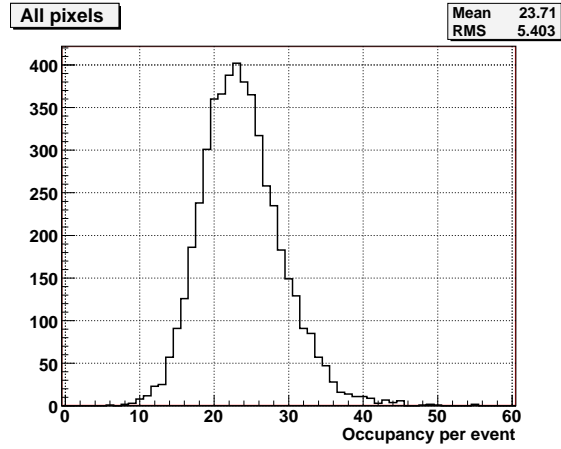


Figure 32: Distribution of total number of pixels per event.

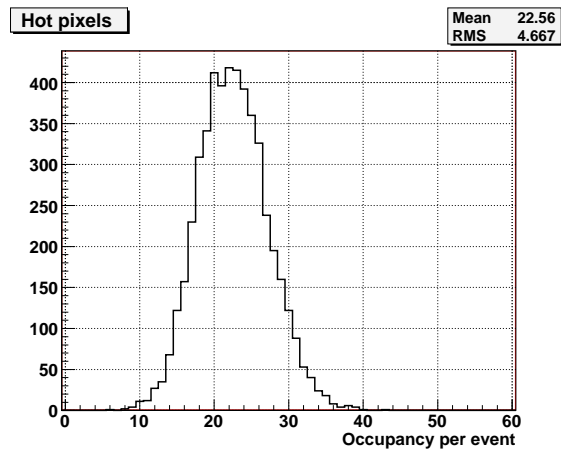


Figure 33: Distribution of number of hot pixels per event.

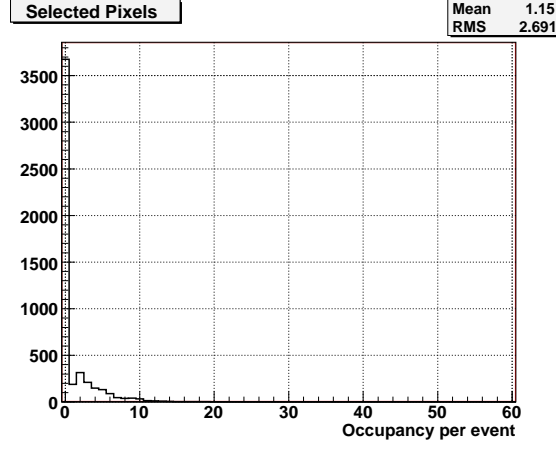


Figure 34: Distribution of number of selected pixels per event.

### 3.2 Results from Run 1129 with Cosmic Trigger

The noise occupancy of run 1129 was investigated through trends regarding the BCID of individual pixel hits to define hot pixels to achieve the highest noise suppression in terms of module noise occupancy (pixel hits per module pixel per event readout). A pixel was classified as hot according to its pixel occupancy, the fraction of pixel hits per event readout as shown in Figure 35. Pixels with an occupancy of  $10^{-5}$  or greater were defined as hot pixels; there were 1547 pixels identified as hot for run 1129, which is roughly 0.023 % of the total pixels in EndcapA.

Analysis of the BCID of hot pixel hits versus the BCID of other pixel hits reveals a relative noise level caused by the noisy hot pixels and a peak at a BCID of 5 for the cold pixel hits as expected from real cosmic track. The module occupancies for all pixel hits shows little consistency across different BCID ranges in Figure 36.

Figure 37 shows the number of hot pixels per module, which reveals some of the noisier modules (layer 0 module 34 and layer 2 module 32). Further investigation of the local position of the hot pixels on module 32 of layer 2 shows an increased density along the boundaries of individual chips in Figure 38.

Removal of hot pixels results in a reduction of noise as predicted earlier through the BCID of hot and cold pixel hits. The module occupancies without hot pixels show much more consistency across BCID and a lower noise occupancy for BCID outside the cosmic signal range, as shown in Figure ???. The module occupancy for outside BCID=4,5,6 range is reduced to the order of  $10^{-10}$ . The increased consistency of module occupancies suggests that the removal of hot pixels results in a better data sample because the noise hits have been reduced to a much lower level.

For the 319 hot pixels on modules not characterized as dead or noisy, 295 were found in a special pixel map denoting certain hardware issues as described in the following section. Most of these pixels have problems relating to the detection of particles and tuning the charge. These pixels were investigated further through cluster and track studies along with clusters completely composed of pixel hits outside the 4,5,6 BCID range. Only 62 tracks out of 15369 were found to contain one or more cluster of this type, which is about 0.4 %. Once these tracks were removed, the overlap efficiency for all three layers rose about 0.2%: a significant raise for such a small removal of tracks.

### 3.3 Results from Run 1131 with Random Triggers

Run 1131 was performed with an external trigger signal at a frequency increasing from 10 Hz to 15 kHz and then decreasing back to 10 kHz. A single level 1 accept signal was used. The number of events in the run is 14 147 494.

The distribution of the occupancies for the individual pixels is shown in figure 40, with the occupancy being defined as the number of hits in a component, in this case one pixel, divided by the number of channels in the component and by the number of events in the run. Taking into account that approxi-

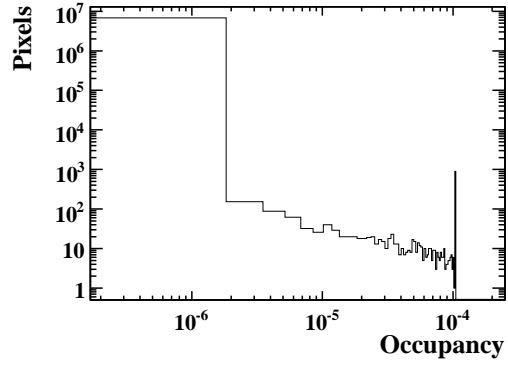


Figure 35: Pixel occupancy per event readout in run 1129.

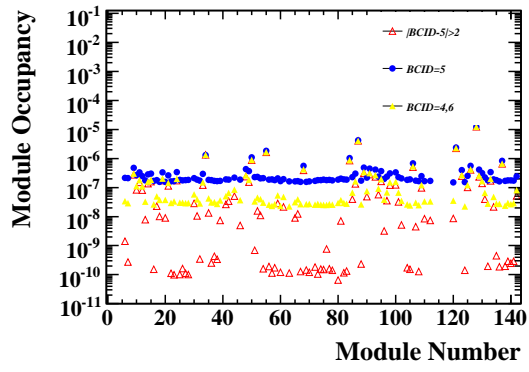


Figure 36: Pixel module occupancy per event readout in run 1129 before removal the hot pixels.

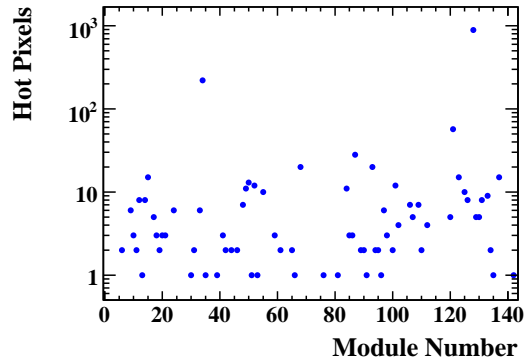


Figure 37: The number of hot pixels per module in run 1129.

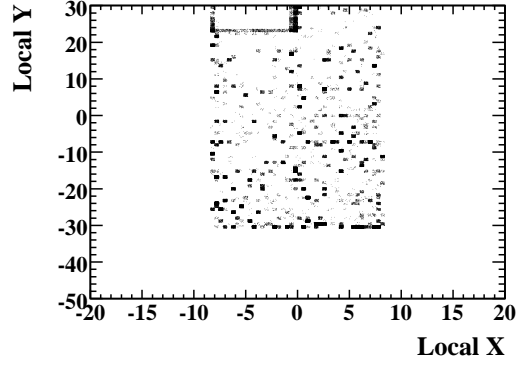


Figure 38: The local position of the hot pixels on one of noisy module 32 of disk 2.

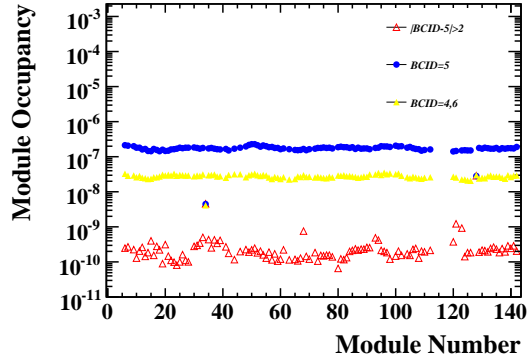


Figure 39: Pixel module occupancy per event readout in run 1129 after removal the hot pixels.

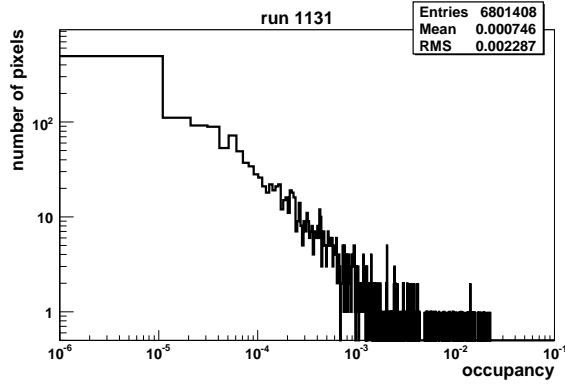


Figure 40: Distribution of the occupancies for individual pixel in endcap A during run 1131. The occupancy is defined as the number of hits in a pixel in the whole run divided by the number of events in the run.

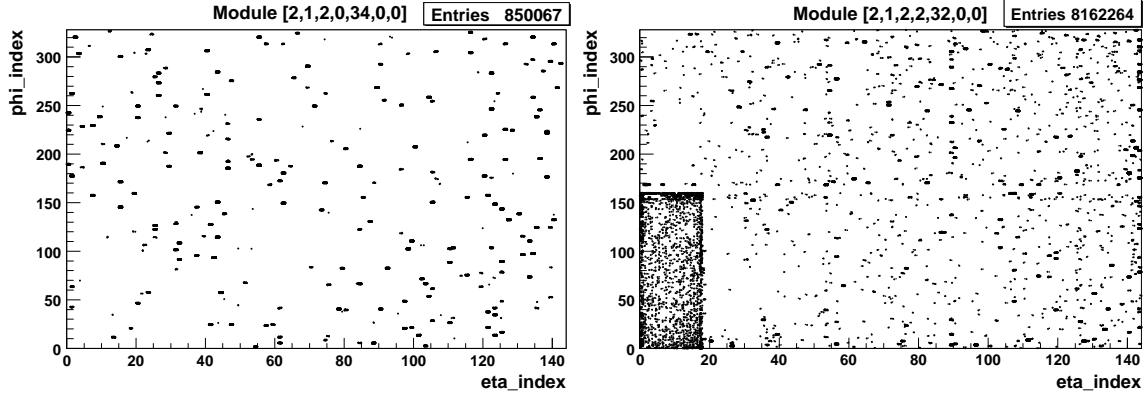


Figure 41: Hit maps for two modules with high noise levels in run 1131.

mately 20 modules were disabled for the run, most of them due to problems with the tuning of the optical readout chain, the occupancy for the endcap in this run is  $2.5 \cdot 10^{-7}$ .

Using the occupancy information it is possible to define pixels as being “noisy”. In the following, all pixels with an occupancy greater than  $10^{-4}$  are defined to be noisy pixels. With this definition there are 871 noisy pixels in endcap A. By excluding the noisy pixels from the analysis the occupancy for the endcap can be reduced by more than 98 % to  $4.8 \cdot 10^{-9}$ .

There were two modules with unusually high noise levels in this run, modules  $[2,1,2,0,34,0,0]$ <sup>1)</sup> and  $[2,1,2,2,32,0,0]$ <sup>2)</sup> which together contained 568 of the 871 noisy pixels. Maps of the hits for those two modules are shown in figure 41. More than 40 % of the hits in the run are found on module  $[2,1,2,2,32,0,0]$ .

The positions of noisy pixels were compared to the positions of pixels that had been marked as being special during the production (“FLEX”) tests of the individual modules. Table 1 gives an overview of the convention for the description of the pixel status used in the offline software and the numbers of pixels with each condition as determined in the production tests. The comparison shows that most of the noisy pixels had been marked as special in the production tests. Excluding the two modules with high noise levels, 283 of the remaining 303 noisy pixels are special, which corresponds to 93 %. 273 of those pixels have bits 0 and 13 set, meaning that the threshold is not tunable and that they do not yield useful data. Table 2 gives an overview of the numbers of status bits for the 303 noisy pixels.

A distribution of the time-over-threshold for all the hits in the endcap is shown in figure 43. One can see that the distribution has a maximum at 5 bunch crossings, or 125 ns, and a tail up to 30 bunch crossings, or 750 ns, and more.

### 3.4 Results from run 1138 with Random Triggers

The run 1138 was taken with an external trigger at a frequency up to 20 kHz and an effective trigger frequency of  $\sim 13$  kHz. 15 231 074 events in this run were analyzed and the results were compared with the special pixel map taken from the production test. 19 modules were masked during the run. Module  $[2,1,2,0,34,0,0]$  was very noisy, and is excluded from the results of the analysis. A total of 23.7 MHits were registered during this run which corresponds to a total occupancy of  $2.7 \cdot 10^{-7}$  per pixel, excluding the 19 masked modules and the noisy one. 51 modules, including the 19 masked ones, didn’t get any hit.

#### 3.4.1 Comparison with the special pixel map

Figure 44 represents the occupancy of pixels both flagged and not flagged as special in the special pixel map. One can see the large occupancy for some of the flagged pixels in the special map. Based on this

<sup>1)</sup>offline ID  $[2,1,2,0,34,0,0]$ , serial number 510853, geographical IDs D1A-S06-M3, D1A-B04\_S1\_M3

<sup>2)</sup>offline ID  $[2,1,2,2,32,0,0]$ , serial number 512876, geographical IDs D3A-S06-M2, D3A-B04\_S1\_M2

<sup>3)</sup>offline ID  $[2,1,2,1,39,0,0]$ , serial number 512951, geographical IDs D2A-S07-M5, D2A-B04\_S2\_M5

<sup>4)</sup>offline ID  $[2,1,2,2,41,0,0]$ , serial number 512429, geographical IDs D3A-S07-M4, D3A-B04\_S2\_M4

bit	meaning	description	numbers of pixels	
			endcap A	detector
0	use code	0 =useful data, 1 =not useful data: black out pixel in reconstruction	4938	129231
1	off for data	set to one if pixel is masked by DAQ	326	5908
2	off for calibration	set to one if pixel is masked during calibration runs	0	0
8	digitally dead	bit 0 of ModuleAnalysis mask: must trigger bit 0	71	57345
9	disconnected bump	bit 1 of ModuleAnalysis mask	1528	29511
10	merged bump	bit 3 of ModuleAnalysis mask	173	1437
11	dead with particles	bit 5 of ModuleAnalysis mask: must trigger bit 0	4173	61852
12	low efficiency with particles	bit 6 of ModuleAnalysis mask: must trigger bit 0	4255	62731
13	threshold not tunable (analog dead)	bit 11 of ModuleAnalysis mask: must trigger bit 0	2675	42567
14	ToT not tunable	bit 14 of ModuleAnalysis mask	2543	37257
15	noisy pixel	bit 16 of ModuleAnalysis mask: must trigger bit 0	17	634
16	unknown dead	any pixel with bit 0 set and bits 8-15 not set	0	2144
25	bottom neighbour special	bottom=smaller row number	3179	90192
26	top neighbour special		3179	90192
27	left neighbour special	left=smaller column number	1624	69386
28	right neighbour special		1624	69386
any	special	pixels that have at least one bit set	5627	141189

Table 1: List of the status bits used to describe the pixel status in the offline software. The pixel status is stored in an unsigned integer, bit  $i$  in the list corresponding to the position  $2^i$  in the integer. The corresponding bits used in ModuleAnalysis, where applicable, are given in column 3. For each bit the number of pixels that were assigned the corresponding status in the production (“FLEX”) tests is given, both for endcap A and for the whole pixel detector. Bits that are not present in the list are not used at the moment.



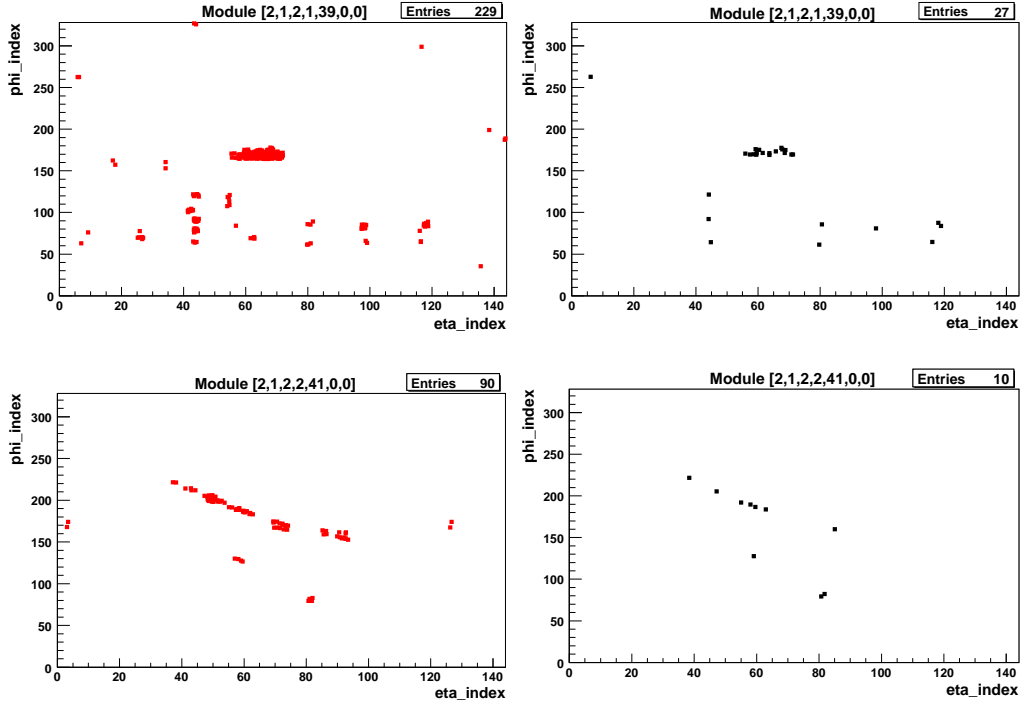


Figure 42: Scatter plots for two modules<sup>3)4)</sup> of pixels marked as special in the production tests (left) and of noisy pixels in run 1131 (right).

status bit	number of noisy pixels	fraction of all noisy pixels
any bit, special	283	93 %
0, not giving useful data	273	90 %
1, off for data	65	21 %
8, digitally dead	0	0 %
9, disconnected bump	0	0 %
10, merged bump	3	1 %
11, dead with particles	205	68 %
12, low efficiency with particles	205	68 %
13, threshold not tunable	273	90 %
14, ToT not tunable	222	73 %
15, noisy	0	0 %

Table 2: Numbers of noisy pixels in endcap A in run 1131, excluding two modules with unusually high levels of noise, for the different status bits as determined from the production test data.

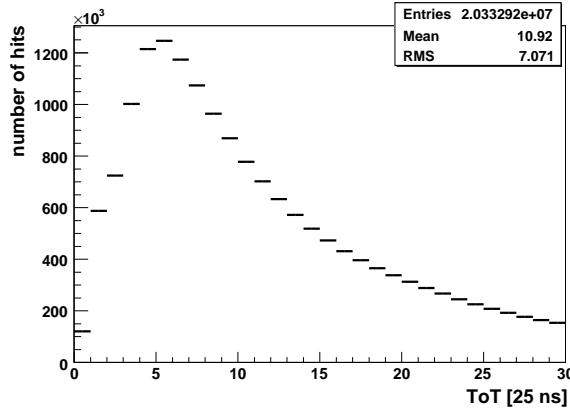


Figure 43: Distribution of the time-over-threshold for all hits in endcap A during run 1131.

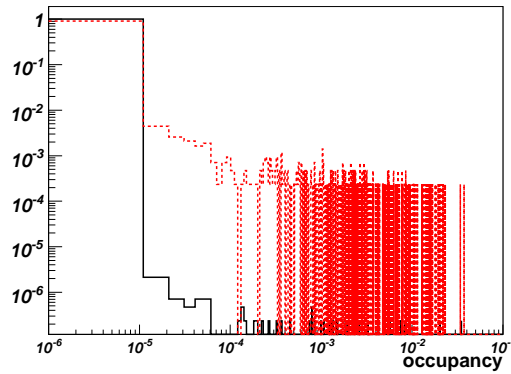


Figure 44: Number of hits per event per pixel. In black solid line pixels that are not flagged in the special pixel map and in red dashed line, for the pixels that are flagged in the special pixel map.

plot, one can define a noisy pixel as a pixel that has an occupancy greater than  $10^{-5}$ . With this definition there are 469 noisy pixels of which 89% were already flagged in the special pixel map. Table 3 shows the number of noisy pixels for different type of pixels according to the special pixel map definitions. If we take into account only modules that have at least one hit<sup>5)</sup>, we can compute the noisy pixel fraction for each special pixel type. Table 4 summarizes this fraction.

### 3.4.2 Comparison with ModuleAnalysis (MA) status bit

Not every type of special pixels in the production test data are copied into the special pixel map. Definition of these types is done using MA. Table 5 summarizes the different status bits in MA and their meaning. The correspondance between MA bits and the special pixel map bits can be found in Table 1. In order to see if one needs to add some other types of pixels to the special pixel map, one has to compare the noisy pixels with the remaining types of pixels that are not copied to this map. Figure 45 shows the pixel occupancy by status bits as defined by both the special pixel map and MA. One can deduce the type of pixels with high noise level. There are 5 types of pixels in MA with a high noise level which are not copied to the special pixel map. This corresponds to bits 7, 8, 12, 13, 15 according to MA definition. If we investigate further, one can see that most of noisy pixels that have these bits set also have another bit that is already in the special pixel map. Table 6 summarizes the fraction of noisy pixels in these bits and the fraction of pixels that have these bits set with no other bit in the special pixel map. For exemple, we can see that for bit 8 (noisy in source test) we have 87% of pixels with no other bit in the special map

<sup>5)</sup>During data taking it was not clear that all modules were working without any problems. So one prefers doing this calculation only for modules that have at least one hit to be sure that they were sending data.

Special pixel map status bit	Number of noisy pixels	Fraction of all noisy pixels
Any bit, special	417	89%
1, off for data	95	20%
8, digitally dead	0	0%
9, disconnected bump	1	~0%
10, merged bump	7	1%
11, dead with particles	299	64%
12, low efficiency with particles	299	64%
13, threshold not tunable	393	84%
14, ToT not tunable	328	70%
15, noisy	1	~0%

Table 3: Number of noisy pixels for the different status bits in the special pixel map and the fraction of these pixels w. r. t. all noisy pixels.

Special pixel map status bit	Noisy fraction of special pixels
Any bit, special	10%
1, off for data	44%
8, digitally dead	0%
9, disconnected bump	~0%
10, merged bump	5%
11, dead with particles	9%
12, low efficiency with particles	9%
13, threshold not tunable	19%
14, ToT not tunable	16%
15, noisy	10%

Table 4: Fraction of noisy pixels w. r. t. all special pixels for the different status bit in the special pixel map.

MA status bit	meaning
0	hits (digital scan)
1	noise difference (HVon -HVoff)
2	noise (or with above)
3	Xtalk fraction (merged bump)
4	Xtalk noise (or with above)
5	source hits
6	source max ToT
7	source masked
8	noise (source scan)
9	difference from mean threshold
10	mean ToT (digital scan)
11	threshold S-fit $\chi^2$
12	leakage currant
13	crosstalk
14	ToT - calibration $\chi^2$
15	overdrive
16	source rate ration

Table 5: Meaning of the different status bit as defined in MA.

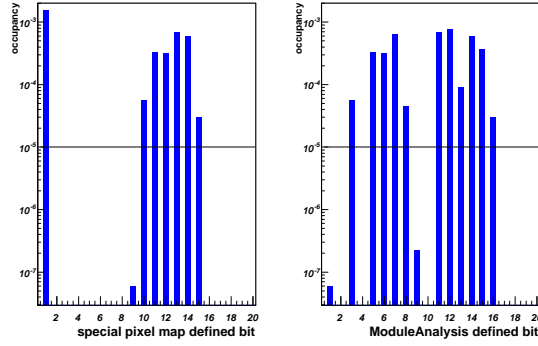


Figure 45: Occupancy per type of pixel for different status bit in the special pixel map and MA.

set. But this number is reduced to 1% if we just look for noisy pixels. That means that the cut used to set this bit was very loose and one should not use it in the special pixel map. All noisy pixels in the other bits are also well covered by the bits of the special pixel map.

### 3.4.3 Occupancy definition for noisy pixels

In this run, we define noisy pixels as pixels with an occupancy greater than  $10^{-5}$ . This definition is rather arbitrary, and the separation between noisy and non-noisy pixels is not clear. If we define noisy pixels as the ones with an occupancy greater than  $10^{-4}$ , instead we get 384 noisy pixels that correspond to 82% of noisy pixels from the first definition. 92% of these pixels are already flagged in the dead pixel map. This number is in complete agreement with the results from run 1131. Table 7 lists the fraction of noisy pixels for different types of special pixels for different occupancy ranges. This table shows that there is no real changes in type of pixels with the occupancy range definition. Figure 46 shows the ToT distribution for noisy and non-noisy pixels for the two occupancy definition cuts. It is clear that the noisy pixels have a higher ToT than normal ones. The discrepancy is very clear for the  $10^{-5}$  definition, while we can see large tails for the non-noisy pixels that seem to be closer to noisy pixels for the  $10^{-4}$  definition.

To investigate further the noisy pixels definition, one can divide pixels in different ranges of occu-

Module Analysis status bit	Fraction of noisy	All pixels not covered in the special pixel map	Noisy pixels not covered in the special pixel map
7, source masked	18%	$\sim 0\%$	0%
8, noisy (source scan)	3%	87%	1%
12, leakage currant	20%	12%	$\sim 0\%$
13, crosstalk	10%	9%	1%
15, overdrive	10%	50%	$\sim 0\%$

Table 6: Status bit as defined in MA and not copied to the special pixel map that contains noisy pixels, with the fraction of pixels that do not have any other bit set in the special map.

Special pixel map status bit	occupancy $> 10^{-5}$	occupancy $> 10^{-4}$	$10^{-5} < \text{occupancy} < 10^{-4}$
1, off for data	23%	22%	28%
8, digitally dead	0%	0%	0%
9, disconnected bump	$\sim 0\%$	$\sim 0\%$	1.5%
10, merged bump	1.7%	1.7%	1.5%
11, dead with particles	72%	73%	66%
12, low efficiency with particles	72%	73%	66%
13, threshold not tunable	94%	96%	86%
14, ToT not tunable	79%	78%	81%
15, noisy	$\sim 0\%$	$\sim 0\%$	0%

Table 7: Fraction of pixels in different bin of occupancy for the different status bits in the special pixel map w. r. t. all pixels in the same occupancy bin.

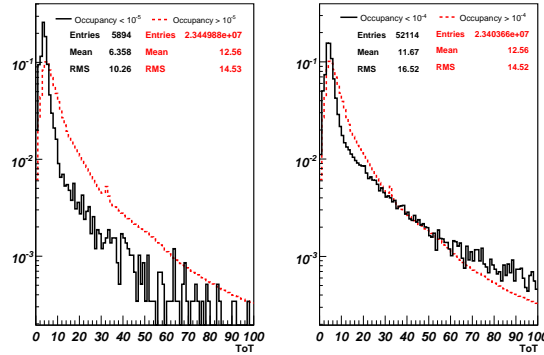


Figure 46: ToT for noisy pixels, in black solid line, and non noisy pixels, in red dashed line. On the right, noisy pixels are defined as the ones that have an occupancy higher than  $10^{-5}$  and on the left, noisy pixels are defined as the ones that have an occupancy higher than  $10^{-4}$ . All distributions are normalized to 1.

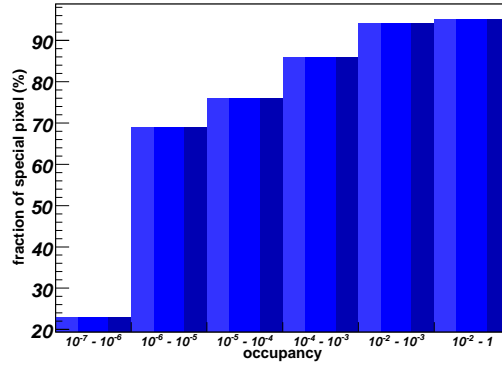


Figure 47: Fraction of pixels that are already flagged in the special pixel map in different occupancy ranges.

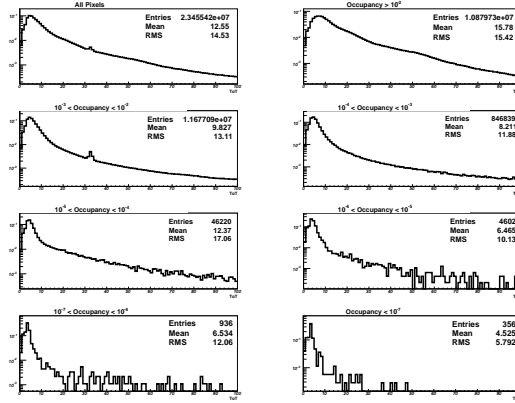


Figure 48: ToT distribution for pixels in different occupancy bins. All distributions are normalized to 1.

pancy. Figure 47 shows the correlation with the special pixel map in different range of occupancy. We can see that almost all pixels with very high occupancy are already flagged in the special pixel map. The fraction of special pixels decreases with the occupancy and there is a large gap at an occupancy of  $10^{-6}$ . One can think that the cuts in the production data test that are used to build the special pixel map correspond to a tight cut on the occupancy ( $10^{-6}$ ) rather than a loose one. Figure 48 shows the distribution of ToT for pixels in different occupancy bins. As expected, one can see that pixels with higher occupancy have a higher ToT. This is not the case for bin  $10^{-5} - 10^{-4}$  where the ToT is higher than expected. If we compare this distribution with the one from bin  $10^{-4} - 10^{-3}$  as shown in figure 49, we can see that the main difference is coming from the large tails in the  $10^{-5} - 10^{-4}$  bin. A fit excluding the tails shows that the mean values in the peak region are comparable. These tails can be explained by one or more pixels that have a higher ToT distribution. This can also explain the tails in the ToT distribution for the pixels with an occupancy  $< 10^{-4}$  in figure 46.

The peak in the ToT distribution in bin  $10^{-2} - 10^{-3}$  is due to one pixel with a strange behavior. The ToT distribution of that pixel is shown in figure 50 for 100000 events.

### 3.5 Results from Run 1153 and 1144 with Special Setting

Run 1153 was performed with an effective trigger rate of about 12 kHz. A single level 1 accept signal was used. The number of events in the run is 16 776 587. In this run, two modules,  $[2,1,2,0,14,0,0]$ <sup>6</sup> and  $[2,1,2,2,27,0,0]$ <sup>7</sup>, had the threshold lowered to TDAC-25, corresponding to a change with respect

<sup>6</sup>offline ID  $[2,1,2,0,14,0,0]$ , serial number 512862, geographical IDs D1A-S03-M2, D1A-B02-S2-M2

<sup>7</sup>offline ID  $[2,1,2,2,27,0,0]$ , serial number 511818, geographical IDs D3A-S05-M5, D3A-B03-S2-M5

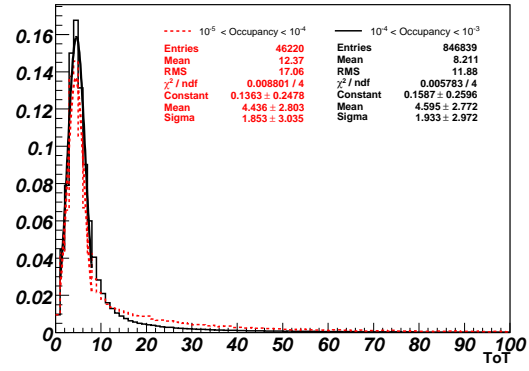


Figure 49: ToT distribution for Pixels with an occupancy between  $10^{-4} - 10^{-3}$  in black solid line and  $10^{-4} - 10^{-5}$  in red dashed line. All distributions are normalized to 1.

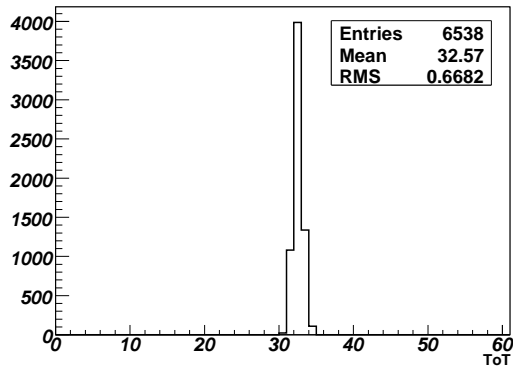


Figure 50: ToT distribution for one of the pixels with a strange behavior that induces a peak in the ToT distribution for all pixels.

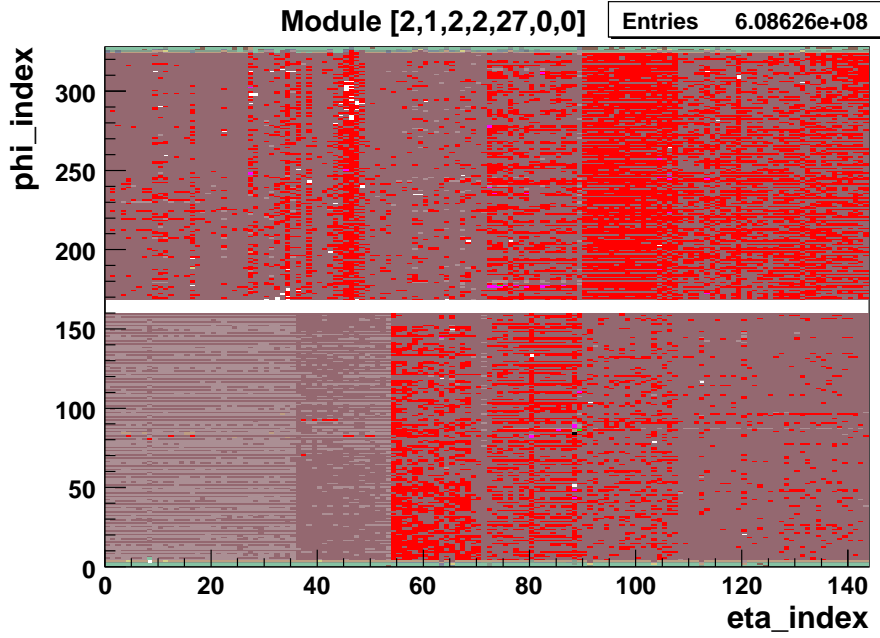


Figure 51: Hit map for module [2,1,2,2,27,0,0] which had a low threshold at TDAC-25 in run 1153.

to the reference value of about 1581 electrons. Module [2,1,2,0,14,0,0] shows an above average number of noise hits, but still has no hits in most of the pixels. Module [2,1,2,2,27,0,0], for which a map of the hits is shown in figure 51, shows a number of about 13 000 hits in almost every pixel. The pixels in the first four rows of every chip, corresponding to a  $\phi$ -index from 0 to 3 and from 324 to 327, show lower than average numbers of hits, with about 6000 hits on average for the first two rows of each chip. This can be seen clearly in figure 52. In a subsequent analysis of run 1144, in which the threshold had been lowered to TDAC-20 for all modules, three modules<sup>8)9)10)</sup> show a similar behaviour in that they have a high number of evenly distributed hits with about half as many hits in the first two to four rows. One module<sup>11)</sup> has a similarly high number of hits but only four front-end chips (0, 6, 8, 15) show a lower number of hits in the first four rows. Hit maps for these four modules with anomalously high noise levels are shown in figures 53 and 54. The other modules in run 1144 exhibit noise patterns that are comparable to those typically found in the runs at default settings except for a higher number of hits in the ganged pixels. Run 1144 contains 16 774 967 events in total taken at a trigger rate increasing from 5 kHz to 13 kHz. A single level 1 accept signal was used.

Several pixels on module [2,1,2,2,27,0,0] show no noise hits in run 1153. The positions of these 82 dead pixels were compared to the positions of the 372 special pixels from the production tests. 61 (74 %) of the 82 dead pixels are special. There are 61 special pixels with the status bits (0,11,12,13,14) set (no useful data, dead with particles, low efficiency with particles, threshold not tunable, ToT not tunable), 57 (92 %) of which are dead. In addition there are 5 special pixels with the status bits (0,1,13,14) set (no useful data, off for data, threshold not tunable, ToT not tunable), 4 of which are dead. These two classes of pixels contain all the pixels with status bit 14 set. None of the 306 special pixels with other combinations of status bits are dead. As this comparison shows, for this module there is an almost one-to-one correspondence between the pixels that show no noise hits and the pixels with status bit 14 set.

Four modules in run 1153 had special TDAC pattern masks applied to them. Modules [2,1,2,1,33,0,0]<sup>12)</sup>

<sup>8)</sup>offline ID [2,1,2,1,34,0,0], serial number 511476, geographical IDs D2A-S06-M3, D2A-B04-S1-M3

<sup>9)</sup>offline ID [2,1,2,1,42,0,0], serial number 512746, geographical IDs D2A-S08-M1, D2A-B01-S1-M1

<sup>10)</sup>offline ID [2,1,2,2,12,0,0], serial number 510392, geographical IDs D3A-S03-M1, D3A-B02-S2-M1

<sup>11)</sup>offline ID [2,1,2,0,10,0,0], serial number 510418, geographical IDs D1A-S02-M3, D1A-B02-S1-M3

<sup>12)</sup>offline ID [2,1,2,1,33,0,0], serial number 512351, geographical IDs D2A-S06-M5, D2A-B04-S1-M5



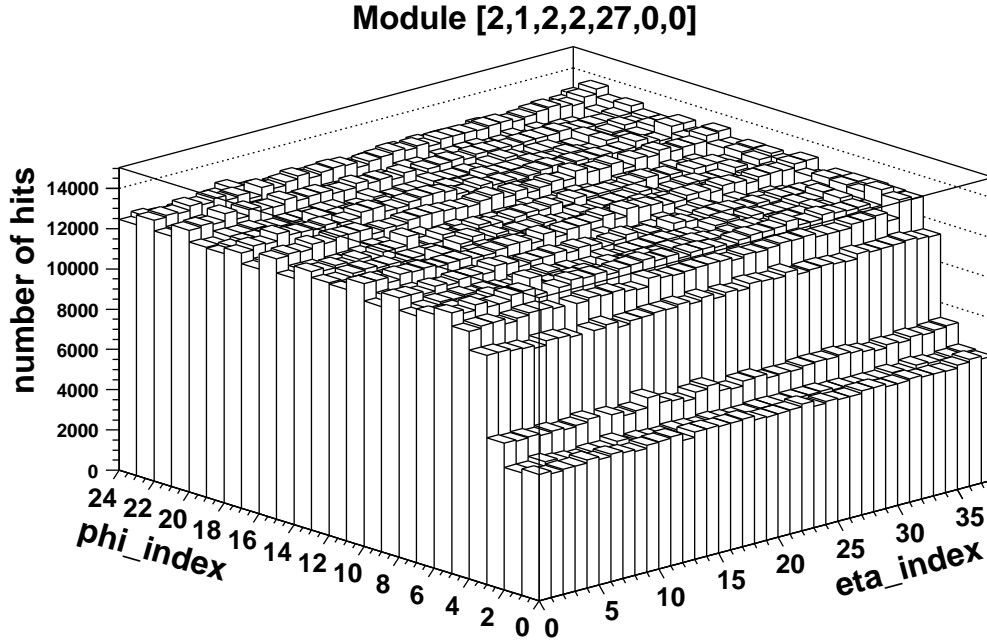


Figure 52: Hit map of a section of module [2,1,2,2,27,0,0] which had a low threshold at TDAC-25 in run 1153.

and [2,1,2,1,14,0,0]<sup>13)</sup> had the mask shown on the left in figure 55 applied to them. The greyscale [17] corresponds to different TDAC settings, black corresponding to TDAC-25 and white corresponding to TDAC+25. No effect on the number of noise hits was observed for these two modules. Almost all pixels on these two modules show no noise hits.

The mask shown on the right in figure 55 was applied to modules [2,1,2,2,44,0,0]<sup>14)</sup> and [2,1,2,0,33,0,0]<sup>15)</sup>. Maps of the hits for these two modules are shown in figure 56. One can see an increased number of noise hits in the areas with the lowest thresholds, especially for the ganged pixels. Since the TDAC pattern mask was applied using column and row numbers instead of eta\_indices and phi\_indices the phi\_index direction has to be flipped for module [2,1,2,0,33,0,0] for comparison with the greyscale image.

### 3.6 Results from run 2043, 2044, and 2045

Runs 2043, 2044 and 2045 were taken with external trigger frequencies of 20KHz, 10KHz, 40KHz respectively. Every run contains about 17 M events and the number of modules with a significant amount of hits ( $>15$ ) is 7. For these reasons a direct comparison of results from these three runs is possible.

#### 3.6.1 Noise level time analysis

Figures 3.6.1, 3.6.1, and 3.6.1 show the number of hit in a module as a function of time, obtained by summing counts within a fixed time interval. The number of intervals is chosen dependently by frequency: it is used a number of 25 steps for 20KHz and 40KHz runs and a number of 50 steps for 10KHz run; this allows the investigation of noise features in the same range of frequencies. The contribution of hot and non hot pixels<sup>16)</sup> is investigated by plotting the same quantities before and after hot pixels removal, since hot pixels contribution is dominant on the normal ones. This permits to underline possible correlations and analogies between noise patterns characterizing hot and non-hot pixels.

<sup>13)</sup> offline ID [2,1,2,1,14,0,0], serial number 512831, geographical IDs D2A-S03-M2, D2A\_B02\_S2\_M2

<sup>14)</sup> offline ID [2,1,2,2,44,0,0], serial number 510559, geographical IDs D3A-S08-M2, D3A\_B01\_S1\_M2

<sup>15)</sup> offline ID [2,1,2,0,33,0,0], serial number 510963, geographical IDs D1A-S06-M5, D1A\_B04\_S1\_M5

<sup>16)</sup> The definitions of hot pixel is as in 3.1

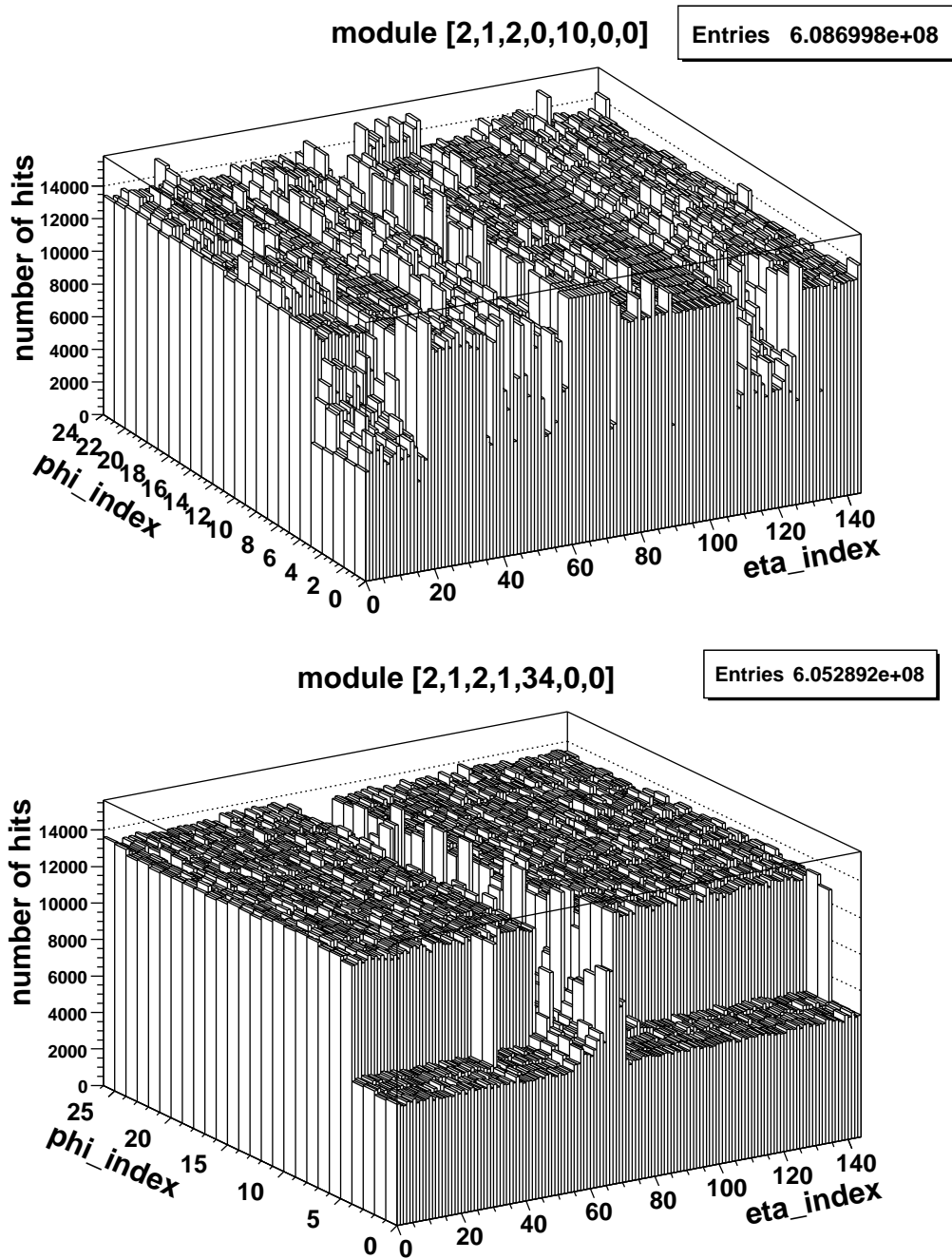


Figure 53: Hit maps of sections of two modules with unusually high noise levels in run 1144, in which all modules had a low threshold at TDAC-20.

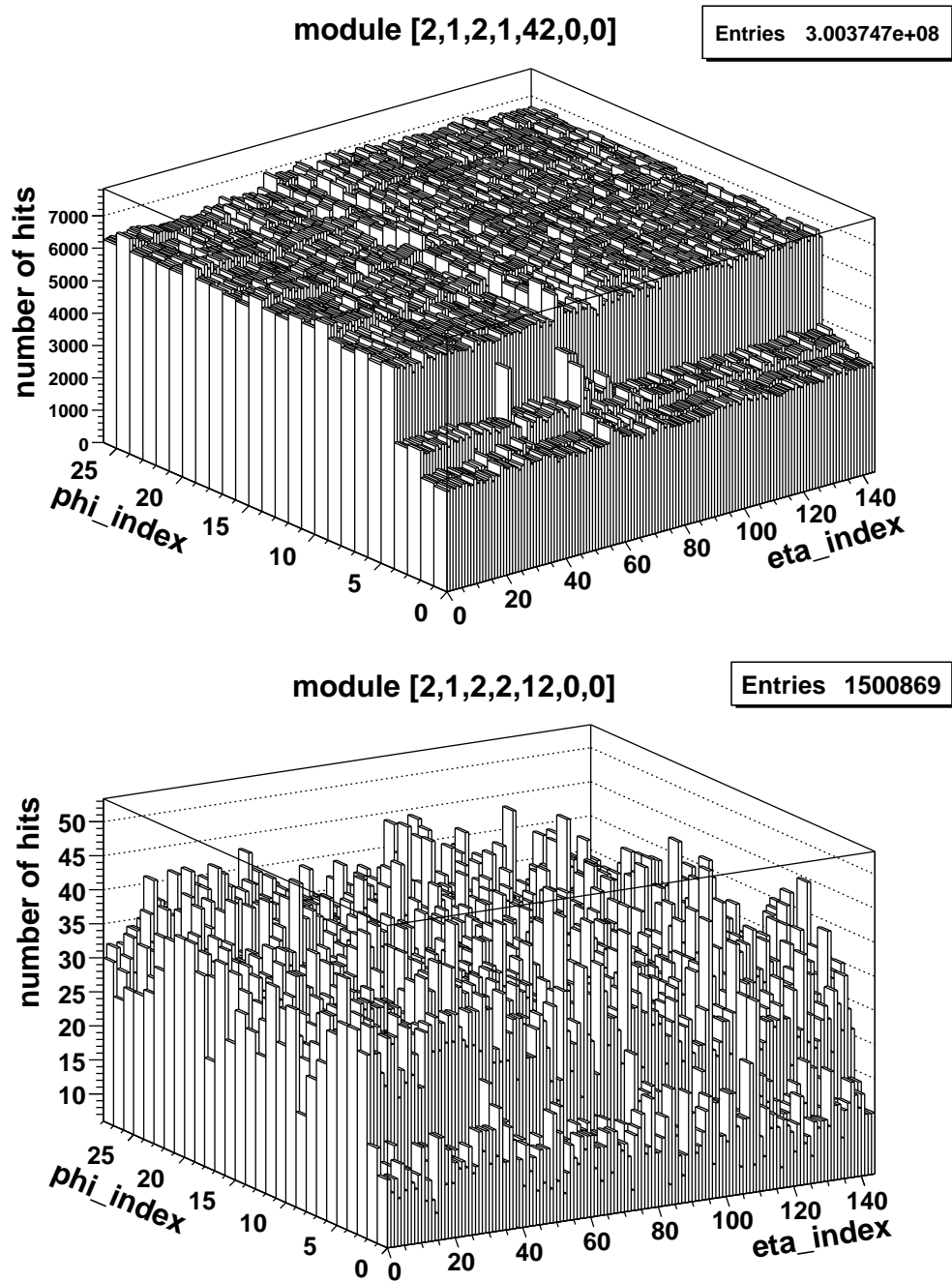


Figure 54: Hit maps of sections of two modules with unusually high noise levels in run 1144, in which all modules had a low threshold at TDAC-20.

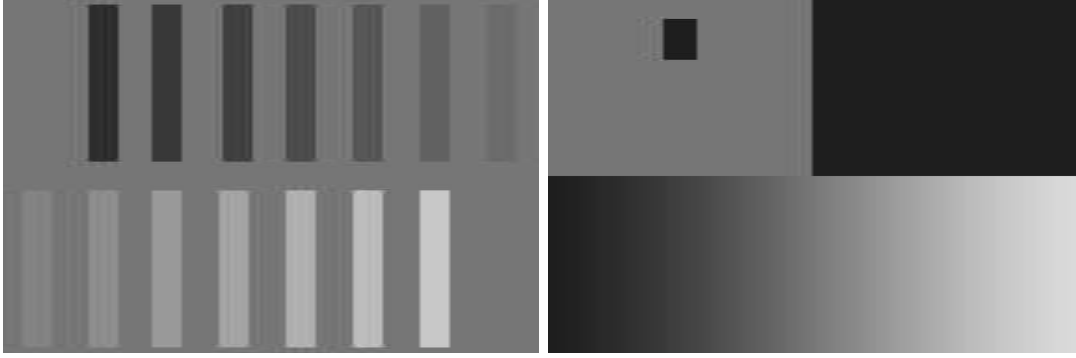


Figure 55: Greyscale images representing TDAC pattern masks that were applied to several modules in run 1153. Black corresponds to TDAC-25, white corresponds to TDAC+25. The mask on the left was applied to modules [2,1,2,1,33,0,0] and [2,1,2,1,14,0,0], the mask on the right was applied to modules [2,1,2,2,44,0,0] and [2,1,2,0,33,0,0].

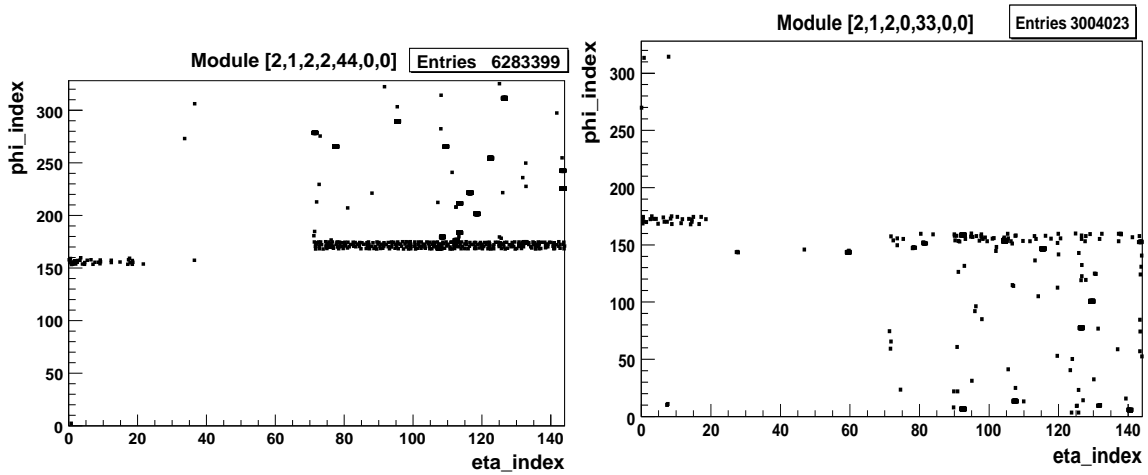


Figure 56: Hit maps for modules [2,1,2,2,44,0,0] and [2,1,2,0,33,0,0] in run 1153 to which the TDAC pattern mask corresponding to the greyscale image shown on the right in figure 55 was applied. Note that the TDAC pattern mask was applied using column and row numbers instead of eta\_indices and phi\_indices and hence the phi\_index direction has to be flipped for module [2,1,2,0,33,0,0].

Three different noise level behaviours can be observed and these features are clearly reproducible from run to run:

- unresolved trend for both kind of pixels as shown in Figure 3.6.1. This is the characteristic of the major part of the module;
- Oscillating pattern with approximately 5 minutes periods<sup>17)</sup> for hot pixel and ambiguous trend for the rest (this ambiguous trend is also due to lack of statistics) as in Figure 3.6.1. The fitting function used is  $[p_0] + [p_1] \sin\left(2\pi \frac{t + [p_3]}{[p_2]}\right)$  where the time is expressed in seconds and the parameter  $[p_3]$  represents the oscillation period in seconds<sup>18)</sup>.
- Module 512779 in Figure 3.6.1 shows a very clear oscillating pattern for hot and non hot pixels. This module is very noisy and contains the 99% of the hits of the whole run. As can be seen from the map of occupancy and hot pixel in Figure 3.6.1, almost all the long pixel are flagged as hot; actually the module was found to have HV off.

Apart from this, no net dependence of noise by time is visible and so the occupancy level of pixels is proved to be stable.

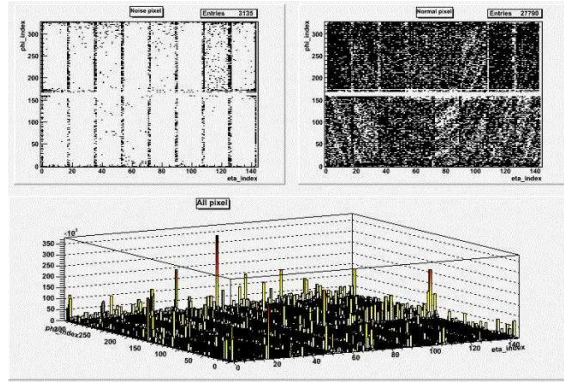


Figure 57: Run 2043 module 1\_23. Hot (top left) and normal (top right) pixel map, hit map (bottom).

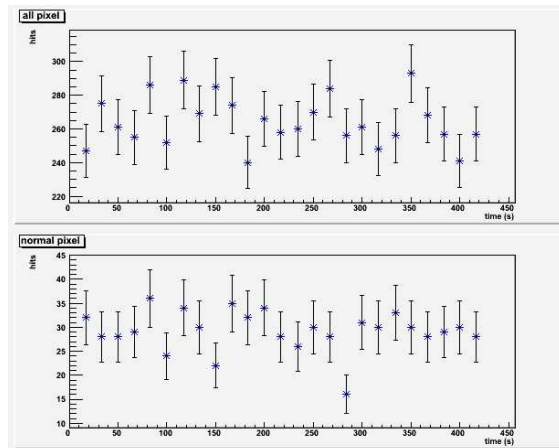


Figure 58: Number of pixel hit as a function of time for all (top) and normal (bottom) pixels on module 0\_18 in Run 2045.

<sup>17)</sup>It is interesting to notice that this oscillating pattern is characterized by a period of approx. (250; 300) s and this fact is independent by the run and the module.

<sup>18)</sup>It is important to notice that the fitting function is chosen only to extract the oscillation period and it is not intended to be used to entirely model the noise patterns. In particular, the function describes only the dominant modulation effect, completely ignoring all the other possible effects which affect the measurement.

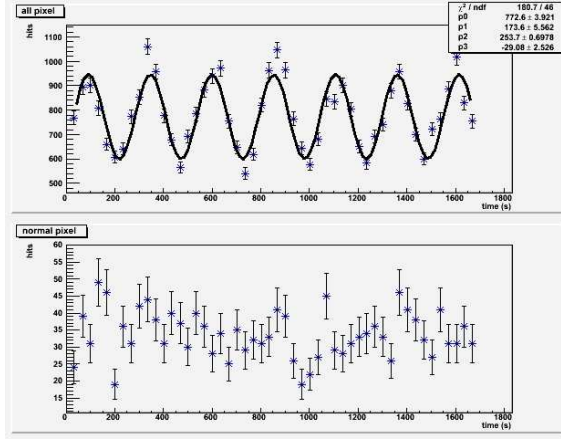


Figure 59: Number of pixel hit as a function of time for all (top) and normal (bottom) pixels on module 0.21 in Run 2044. The fitting function shows the clear evidence of a modulation of the hot pixel noise.

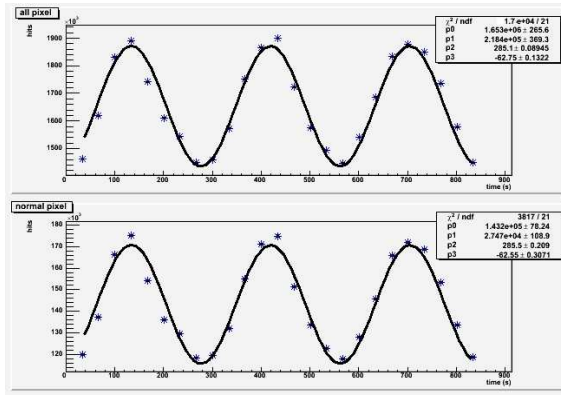


Figure 60: number of pixel hit as a function of time for all (top) and normal (bottom) pixels on module 1.23 in Run 2043.

### 3.6.2 Noise level frequency analysis

Run executed at constant data taking frequency are also aimed to study the way the noise level is connected to the rate of data out the detector. Since the number of events in all the runs is approximately the same, it is sufficient to look at the hit in every module in order to compare the occupancy.

The results are summarized in table 8 in which only the meaningful modules are taken into account (the noisy module described in 3.4.1 is not considered). As in the previous analysis, data are considered before and after hot pixels removal. An interesting fact is that, after the removal procedure, there is still a broad range of hits per module. This may suggest that the cut in occupancy which define hot pixels is in some sense arbitrary and can not be so sharp. The number of hits on the same module in different runs is almost the same and the differences are within few percent. This result suggests that the noise level has a weak correlation with frequency in the range analyzed.

## 3.7 Summary

The noise in endcap A of the pixel detector was studied for several exemplary runs with different detector settings. The analysis of noise in the cosmics data run 1125 shows that the noise signal, as expected, is uncorrelated with the timing relative to the trigger signal and that the noise is dominated by *fixed pattern* noise, i.e. by hits in a relatively small number of noisy pixels. After removal of the noisy pixels the noise occupancy for the endcap is of the order  $10^{-9}$ . This result for the occupancy is confirmed in an analysis of the noise run 1131 in which a random trigger signal was used. A comparison shows that most of the noisy pixels in this run were found to be *special* during the production tests of the individual modules. An analysis of modules with a low threshold setting in runs 1153 and 1144 shows a moderate

<i>Module</i>	<i>Run 2043 (all hits)</i>	<i>Run 2043 (normal hits)</i>
0_18	6401	782
0_19	141696	—
0_20	6120	1375
0_21	40411	1646
1_18	9045	2
1_20	298123	6233
	<i>Run 2044 (all hits)</i>	<i>Run 2044 (normal hits)</i>
0_18	6271	770
0_19	141374	5
0_20	6194	1355
0_21	39220	1683
1_18	9062	—
1_20	297561	5994
	<i>Run 2045 (all hits)</i>	<i>Run 2045 (normal hits)</i>
0_18	6393	731
0_19	141642	—
0_20	6081	1417
0_21	42576	1597
1_18	9102	—
1_20	302266	6330

Table 8: Number of pixel hit per module for all and non hot pixel in each run. The module number is derived from the following convention: nLayer\_nPhi where nLayer represents the disk and nPhi the module's phi angle.

increase in the number of noise hits, especially in the ganged pixels. Several modules in these runs show an atypically high level of noise with the unexpected feature that the noise level in the first two to four rows of most front-end chips is only about half as high as in the other rows.

## 4 Timing studies for cosmic trigger

An important features we managed to check during the cosmic data taking is the synchronization of the modules. The study of LVL1 distribution has been used to measure relative synchronization of modules with a resolution better than 1 ns. Infact different value of delay corresponds to different shape of the bunch crossing distribution. Using simulation we built a function that fit the BCID plot giving an estimation of the delay. First of all we generated the BCID plot for delay from 0 to 400 ns and we calculated the fraction  $F_N$  of hits in a given bin  $N$  of the BCID plot as a function of the delay. For any bin the fraction can be obtained considering that

$$F_N(t) = F_{N-1}(t + 25) = F_{N-2}(t + 50) = \dots \quad (2)$$

and

$$F_N(t) = F_{N+1}(t - 25) = F_{N+2}(t - 50) = \dots \quad (3)$$

The different mean incidence angle affects the charge collection and therefore the timewalk and the hit arrival time so it has been necessary to make the function  $F_N(t)$  for each module. Then we provided a function that fit BCID plot:

$$\psi(BCID) = n + h \cdot F_N(d + (N - BCID) \cdot 25) \quad (4)$$

where  $BCID$  is the variable,  $N$  is a reference  $BCID$  used to build  $F$  and the paramaters are:

- $n$  is the noise probability i.e. number of hits per bunch crossing

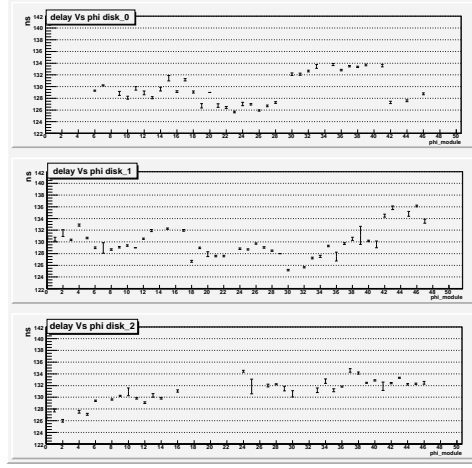


Figure 61: The fitted delay time for each module on three endcap disks obtained from the run 1129.

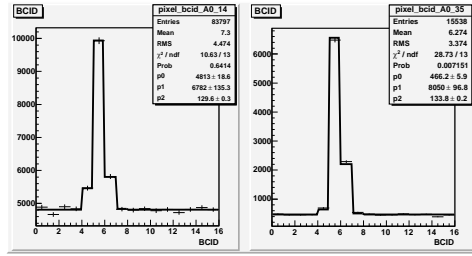


Figure 62: Comparison of fitted BCID distributions for module 14 and 35 of disk 0 that has very different time delays.

- $h$  is the number of hit from a track in the plot
- $d$  is the delay value

Tests of the algorithm fit on montecarlo data (with no asynchronous modules) give satisfactory results, infact we obtained a distribution for the parameter  $d$  (delay), with sigma less than 1 ns and pull functions RMS of 1.15. The results of the fit for the run 1129 are shown in figure 61. The estimated delay is plotted for each phimodule values on three endcap disks. The plot shows that some module are delayed in comparison to the others; the delay we notice is not a problem of the fit infact, as shown in figure ?? where BCID for two module with different delay are plotted as example, we have a very good agreement of the fit. Most part of the modules is well fitted by the function.

## 5 Cosmic Tracking Studies

The offline release used for the cosmic analysis is 12.3.0 including the latest fixes of the bytestreamer converter from InDetTB04ByteStream-00-00-52 and PixelIMap from InDetCabling-00-03-27. Pixel clusters were reconstructed using a simple clustering algorithm where all adjacent hits sharing at least one of sides were clustered together. The cluster position in the local x and y coordinators was computed using a charge weighted centroid with an uncertainty assigned as the pitch divided by  $\sqrt{12}$ . For cosmic tracking, we use the modified existing CTBSiTracking package [18]. First the algorithm loops over any pair of the pixel clusters from the inner and outer disk and linearly extrapolates to the middle disk. If there is a pixel cluster found within a search window of 1.5 mm in the middle disk, a cosmic track is reconstructed successfully. Then repeating the search to add overlap hits from the neighboring module. Finally, the best track is selected using SiCTBAmbSolver, which is based on the number of pixel clusters and the fitted chisq ( $\chi^2 < 25/\text{ndof}$ ) in the x-z and y-z plane. The output track collection is saved as



Table 9: The rate of cosmic tracks found in data and various Monte Carlo samples.

Data Sample	Tracking Rate (%)	Overlap Fraction (%)
Data	$2.83 \pm 0.01$	$23.4 \pm 0.2$
Ideal MC	$\approx 6$	$\approx 28$
Realistic MC(disable modules)	$3.9 \pm 0.1$	$24.6 \pm 0.9$

“SCT\_Cosmic\_Tracks” and there is no ESD or AOD written out, but CBNTs are saved that contain all the information about pixels, clustering, and tracking for data analysis. Initially, there were couple problems found. For example, the channels of odd modules were in the wrong order, and the ganged pixels were not included properly. But they were quickly fixed after checking some basic quantities, like the minimum distance between the expected and the actual hits nearby shown in Figure 63 and the residuals between two overlap hits in adjacent modules shown in Figure 64 before and after the fix, respectively.

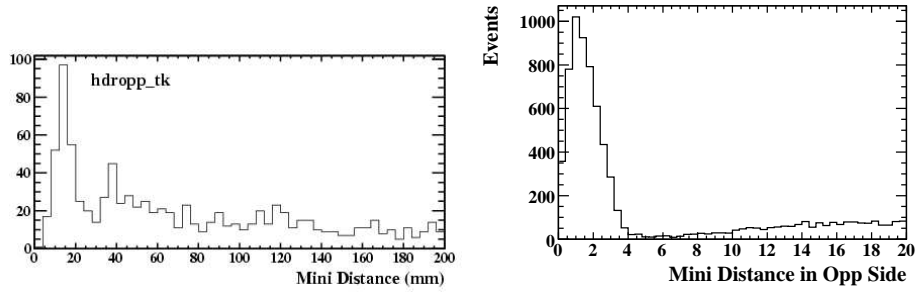


Figure 63: The minimum distance between the expected position and the nearby hits before (left) and after (right) fixing the readout order for the odd modules in the back of the disk.

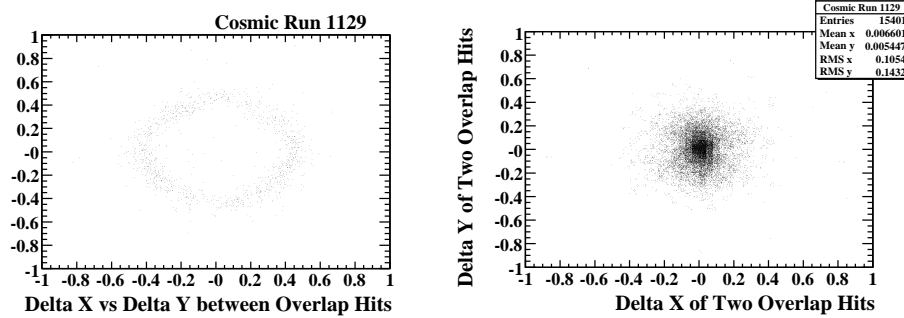


Figure 64: The scatter plot of dx and dy between the overlap hits before (left) and after (right) fixing the missing 8 ganged pixels in PixelIMap.

In order to better understand the detector performance, we have generated cosmic Monte Carlo with a realistic detector simulation that contains a list of modules that were disabled during the data taking. However, we still have not taken into account the special pixel map yet. So the simulation results are still optimistic comparing to the data.

Table 9 summaries the tracking rate per event and the fraction of tracks with overlap hits ( $\geq 4$  pixel hits) in the data and the Monte Carlo with different conditions. The overall tracking rate is 2.83% in data, which is lower than realistic MC 3.9%. However, the fraction of overlap hits are consistent between data and Monte Carlo, which indicates data and Monte Carlo have comparable pixel hit efficiencies.

Figure 65 shows the number of pixel clusters, total chisq, phi and theta of the reconstructed cosmic tracks. The agreement between data and Monte Carlo are quite good, except a spike in phi distribution caused by some noised modules in the data. We also checked the quality of clusters associated with the

reconstructed track, which are shown in Figure 66 on the time over threshold (TOT or charge), the cluster width, beam cross trigger identifier (BCID), and the module occupancy as function of  $\phi + 48 \cdot \text{Layer}$  where  $\phi$  is the module number between 0 to 47 and Layer is the disk number between 0 to 2. A nice Landau peak is clearly visible. However, the TOT is somewhat shifted to higher side compared to the Monte Carlo prediction that was tuned based on the test beam data. This is not understood yet. Two noise modules were clearly visible in Layer 1 and Layer 2, which causes a spike in the  $\phi$  distribution of reconstructed tracks.

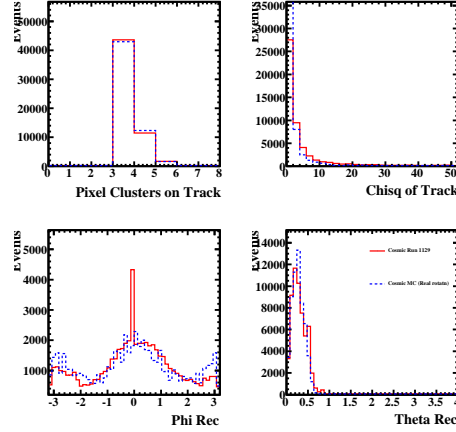


Figure 65: The comparisons of cosmic tracking in terms of the number of pixel hits (top left), the chisq of fit (top right), the  $\phi$  and  $\theta$  of the reconstructed cosmic tracks (bottom left and right ). The solid curve is data and the dashed one is Monte Carlo.

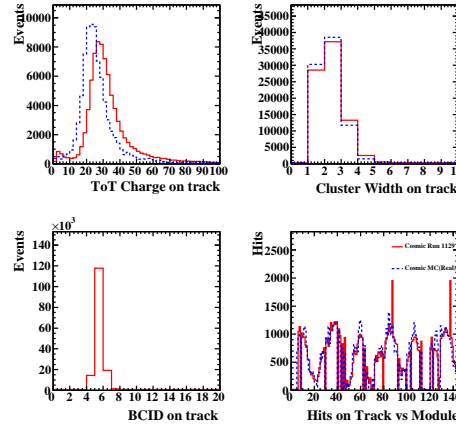


Figure 66: The comparisons of cosmic tracking in terms of the TOT (top left), the cluster width(top right), the beam crossing (BCID) and the module occupancy (bottom left and right ). The solid curve is data and the dashed one is Monte Carlo.

## 6 Pixel Clustering and Efficiency Studies

In this section, we present a study of pixel clustering and hit efficiency using the tracks found in the pixel endcapA cosmic data. The quantities we have looked at are the pixel cluster width and the charge as a function of track incident angle. The cluster width and charge would increase as the incident angle becomes larger. Figure 67 shows the pixel cluster width in the local  $x$  (width $_x$ ) direction for all the clusters found on the cosmic tracks as function of the incident angle ( $\tan(\theta) \cdot \cos(\phi - \phi_m)$ ) where  $\theta$  and

$\phi$  is the reconstructed track parameters and  $\phi_m$  is the module  $\phi$  in the global frame. The top left and right plots show the data and the Monte Carlo. The bottom left plot shows the projection of the cluster widthx and the bottom right plot shows the profiling of the cluster widthx vs the incident angle. Overall, the data agree with the Monte Carlo very well, except the noise clusters from some noisy modules identified as module/layer: 15/0, 34/0, 39/1, 25/2, and 41/2. After imposing a simple clean up by excluding all the tracks that uses the cluster from these noisy modules, we lost about 17% of tracks. Figure 68 shows the same plot after clean up, which are effectively removed all the noisy clusters. For the rest of the studies, the clean up is applied unless noted otherwise.

Figure 69 shows a similar plot, the cluster width in local y (widthy) as function of the incident angle. Since the pixel pitch size in local y is much larger than in local x, the widthy of pixel clusters is expected to be much smaller. The data is in good agreement with Monte Carlo expectation. The cluster charge (TOT) is also plotted as function of the path length through the silicon, which is shown in Figure 70. As noted in the previous section, the peak seems shifted in the Monte Carlo due to a wrong pixel calibration used in the simulation, but the shape seems very similar. We also checked the cluster “analogy” position, which is defined as  $x_{ana} = x_{dig} + k * (\eta - 0.5)$  where  $\eta$  is the ratio of Tot charge in the largest row to the sum of Tot on the largest and the lowest row in the pixel cluster and k is a constant factor, dependent on the track incident angle. Figure 71 and 72 show the scatter plot of  $\delta x_{ana}$  and  $\delta \eta$  between the pixel clusters in the left and right overlap regions, respectively. There seems a good agreement between data and Monte Carlo, but clearly the k needs an additional correction of  $24 \pm 4 \mu m$ .

Since there is no specific requirement of the overlap hits used in the current cosmic tracking, we can use that to measure the pixel hit efficiency properly by checking how often a pair of hits found in the overlap region when the one is expected. We first start with a hit from a track that is on one side of the disk and extrapolate it to the other side of the same disk. If the expected hit is inside a fiducial region of an active module, we then try to match it to a real pixel hit in that module that has a minimum distance ( $drmin = \sqrt{(\delta x^2 + \delta y^2)}$ ). If there is no hit or drmin is larger than 5 mm, we reset drmin to 4.9 mm. Figure 73 shows the drmin distributions from each disk in the data that agrees well with the Monte Carlo. The efficiency is found to be close to 99.5% for all three disks by requiring  $drmin < 1.0$  mm. Figure 74 shows the efficiency as function of module number (0-143), which indicates most of modules are close to 100% efficient.

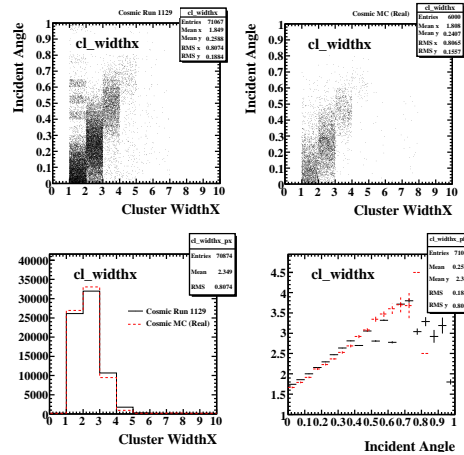


Figure 67: The distributions of pixel widthx for all the clusters found on the track as function of incident angles: top left and right are the data and the MC; bottom left is projection of pixel widthx; bottom right is profiling widthx as function of the incident angle.

## 6.1 Pixel Cluster Width vs Genant4 Cuts in Simulation

In order to understand better the pixel clustering simulation in Monte Carlo, we have made a comparison of the cluster size distribution of clusters associated to a track between data and simulation with different Geant4 cuts. Figure 75 shows the mean cluster size as a function of the incident angle where Red points

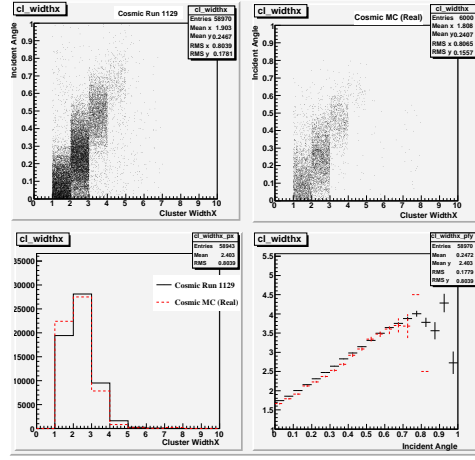


Figure 68: The distributions of pixel widthx for all the clusters found on the track as function of incident angles after noise clean up: top left and right are the data and the MC; bottom left is projection of pixel widthx; bottom right is profiling widthx as function of the incident angle.

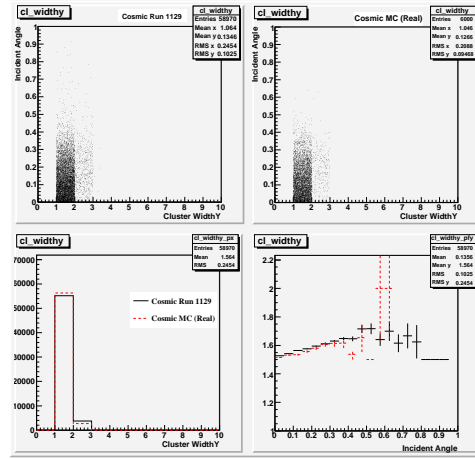


Figure 69: The distributions of pixel widthy for all the clusters found on the track as function of incident angles after noise clean up: top left and right are the data and the MC; bottom left is projection of pixel widthy; bottom right is profiling widthx as function of the incident angle.

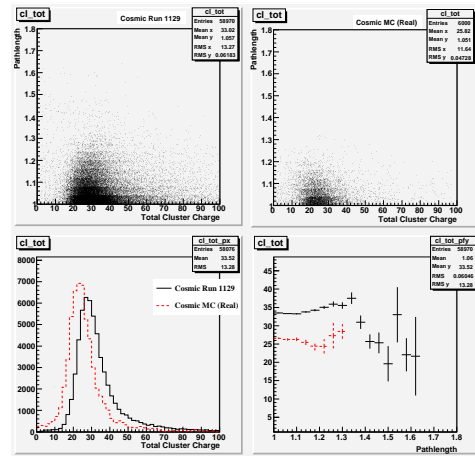


Figure 70: The distributions of Tot for all the clusters found on the track as function of incident angles after noise clean up: top left and right are the data and the MC; bottom left is projection of Tot; bottom right is profiling Tot as function of the incident angle.

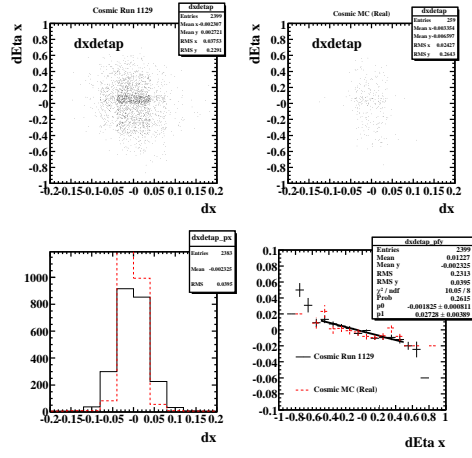


Figure 71: The scatter plot of  $\delta x$  and  $\delta \eta$  between the overlap hits in the right overlap region: the top left and right are the data and the Monte Carlo; the bottom left plot is the projection of  $\delta x$  and the right plot is the profiling of  $\delta x$  vs  $\delta \eta$ . A line of fit gives a slope of  $27.3 \pm 4 \mu m$ .

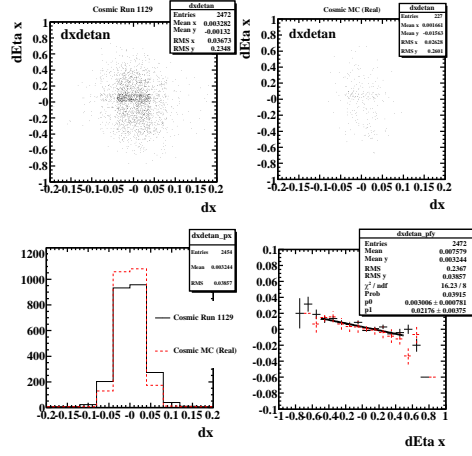


Figure 72: The scatter plot of  $\delta x$  and  $\delta \eta$  between the overlap hits in the left overlap region: the top left and right are the data and the Monte Carlo; the bottom left plot is the projection of  $\delta x$  and the right plot is the profiling of  $\delta x$  vs  $\delta \eta$ . A line of fit gives a slope of  $21.8 \pm 4 \mu m$ .

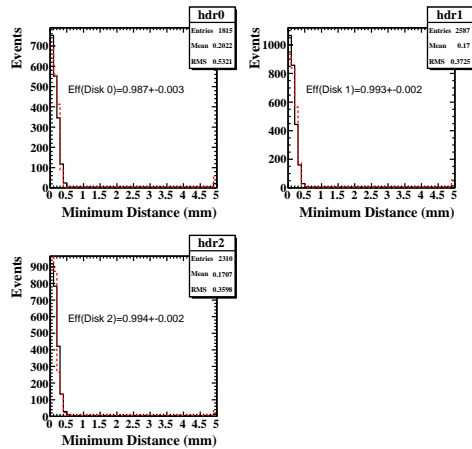


Figure 73: The distributions of the minimum distance between the expected and real pixel hits in the overlap region for three disks in the data (histogram) and in the Monte Carlo (red dash histograms).

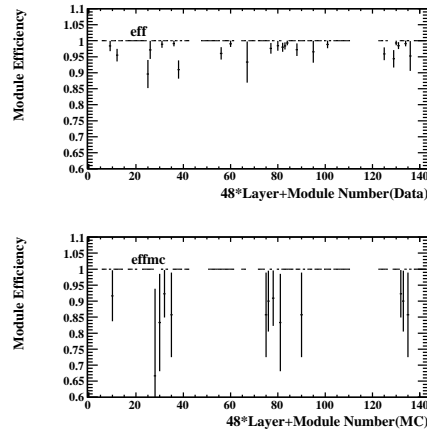


Figure 74: The pixel hit efficiency as function of module number (0-143) in the cosmic data (top) and in the Monte Carlo(bottom).

are the data from run 1129, black ones are the simulation with the default parameters (which are  $1000 \mu m$  for the cut on the range of secondary events and no step limitation), blue points refer to the simulation with the cut on the range of secondary events of  $100 \mu m$  and the maximum step length of  $100 \mu m$ , green points refer to a simulation with the cut on the range of secondary events of  $50 \mu m$  and the maximum step length of  $50 \mu m$ .

There seems that a smaller cut on the range of secondary events increases the mean cluster size for small incident angles. On the other side there seems that decreasing the step limitation, introducing Landau fluctuations, decreases the mean cluster size, as if we miss one hit. There is a strange behaviour that we still have to understand. For small incident angles, the simulations with non default G4 cuts seem describe the data better but it seems that for bigger incident angle the default simulation is more similar to the data.

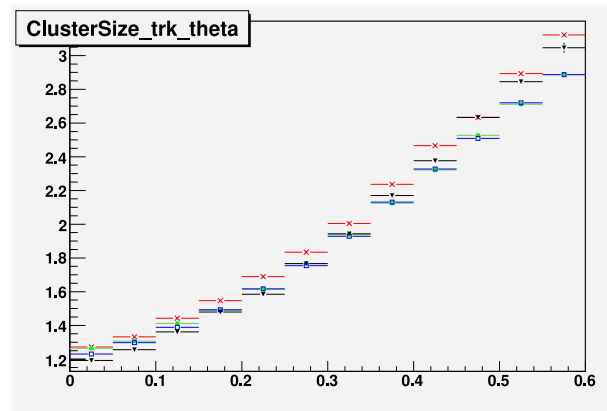


Figure 75: The mean cluster size as a function of the incident angle where Red points are the data from run 1129, black ones are the simulation with the default parameters (which are  $1000 \mu m$  for the cut on the range of secondary events and no step limitation), blue points refer to the simulation with the cut on the range of secondary events of  $100 \mu m$  and the maximum step length of  $100 \mu m$ , green points refer to a simulation with the cut on the range of secondary events of  $50 \mu m$  and the maximum step length of  $50 \mu m$ .

## 6.2 Overlap Efficiency vs Disabled Pixels

We have recomputed the efficiency in overlap regions as function of different geometrical cuts (on x-axis the y-intercept of the oblique line which defines the overlap area), as shown in Figure 76. Results are similar for all choices, even if the error is greater as the overlap area decreases, due to lower number of hits.

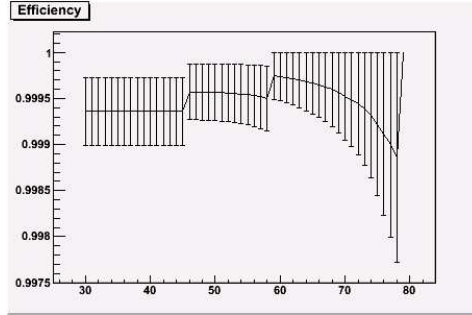


Figure 76: The efficiency in overlap regions as a function of the geometrical cut (on x-axis the y-intercept of the oblique line which defines the overlap area) for simulated sample.

A simulated sample of data with a random noise equal to  $1.34 \cdot 10^{-8}$  (similar to run 1129) give us an efficiency of  $0.9994 \pm 0.0004$ , as expected, since in simulation efficiency was set equal to 1. To check the algorithm used, we produced sample of simulated data with different values of fraction pixel disabled in the event. Efficiency decreases as the percentage raises, as expected, which is shown in Figure 77. The decrease in efficiency is less than disabled pixels. This fact is still to be understood quantitatively, but it seems due to the size of clusters: even if a pixel is disabled, nearby another pixel can still collect charge to make a hit.

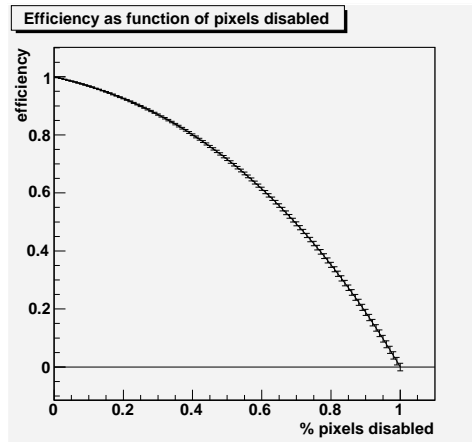


Figure 77: Efficiency between modules of the same disk as a function of the number of disabled pixels.

## 7 Alignment with Overlap Residuals

There are about 24% of tracks containing an overlap hits from neighboring modules, which can be used to check the relative alignment between adjacent modules. Before doing so, we need to make sure the noise contamination of overlap hits are small, as shown in Figure 78 for the overlap hits in terms of the module occupancy, xy scatter plot, track phi and a scatter plot of TOT vs the fitted track chisq. As expected, the tracks with overlap hits seem much more reasonable, and pure compared with the Monte Carlo.

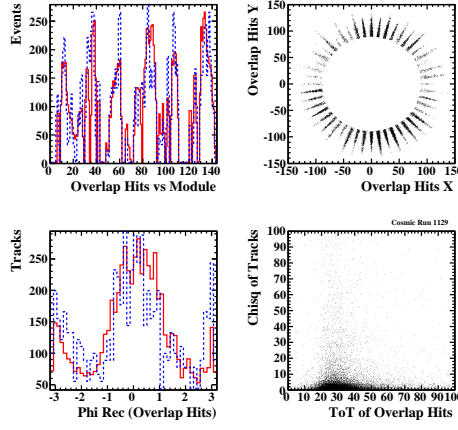


Figure 78: The distributions of the overlap hits in terms of the module occupancy (top left), xy scatter plot (top right), track phi (bottom left) and a scatter plot of TOT vs the fitted track chisq (bottom right). The solid is for the data and the dash is for the Monte Carlo.

Assuming the module as a rigid body, there are 4 parameters to describe the module position inside the disk:

- Shift  $X_0$  in local X axis along the short pixel direction
- Shift  $Y_0$  in local Y axis along the long pixel direction
- Shift  $Z_0$  in local Z axis perpendicular to the disk
- Rotation  $\alpha_0$  along local Z axis

The relative alignment constants were determined considering the difference  $\Delta x$  and  $\Delta y$  between the positions of the overlap hits in the local reference plane of the odd module after taking into account the track extrapolation. Figure 79 shows the overlap residuals vs the number of odd modules in the left and right overlap regions. The  $dX_0$  and rotation  $d\alpha_0$  were determined by a line fit of  $\Delta x$  vs local Y of the hit in the odd module. The  $dY_0$  were determined from the mean of  $\Delta y$ . The  $dZ_0$  were determined by a line fit of  $\Delta x$  vs  $\tan\theta \cdot \cos\phi$  where  $\theta$  and  $\phi$  are the angles of the reconstructed cosmic track. The overall residuals before and after alignment correction are shown in Figure 80 with a nominal geometry with  $dz = 4.25$  mm, instead of 4.2 mm. The resolution in LocX improves from 21.2 to 17.8  $\mu m$  while the resolution in LocY remains the same at 117  $\mu m$ . Figure 81 summarizes the relative alignment constants as a function of odd modules in the left and right overlaps regions. Most of them are within 20  $\mu m$ , which indicates the pixel endcapA is well reconstructed.

We have also checked the residuals with the endcapA as built survey geometry [20], which has slighter better resolution of 20.7  $\mu m$  than the one with nominal geometry. In order to check the correlation between the alignment constants and the survey data, we select the modules with more than 50 overlap hits and compare the relative alignment constants as shown in Figure 82, which seems indicate some correlations do exist between the alignment and survey, but not as strong as we hoped. Another interesting test is to check the relative alignment between modules in both front and back adjacent modules in the same sector or different sectors since the survey is conducted much more accurate for the front modules in the same sector than the back modules or modules in cross different sectors. Figure 83 shows the comparison between the alignment and the survey data. Again, they seem correlated in some degree. At this moment, it would be difficulty to derive absolute alignment constants for the modules within the disk since some of modules were not function during the cosmic data taken. However, the results are quite impressive for what we have achieved so far with such limited data. Some of difficulties are due to limited data statistic or some of unknown systematic which we have not uncovered yet.



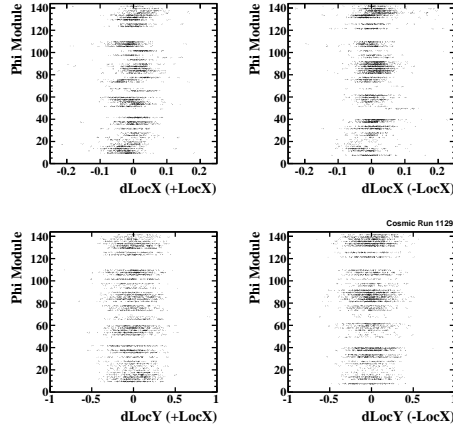


Figure 79: The overlap residual distributions as function of module number (module+48\*Layer): residual X in +LocX and -LocX of odd modules (top) and residual Y (bottom).

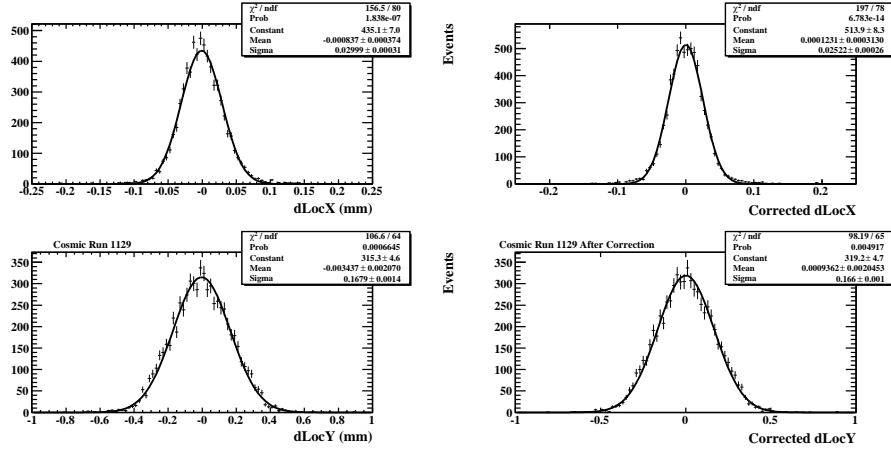


Figure 80: The overlap residual in LocX and LocY with nominal geometry with  $dz=4.25$  mm (left) and after alignment correction (right). The resolution is  $1/\sqrt{2}$  of the residual shown in the plot.

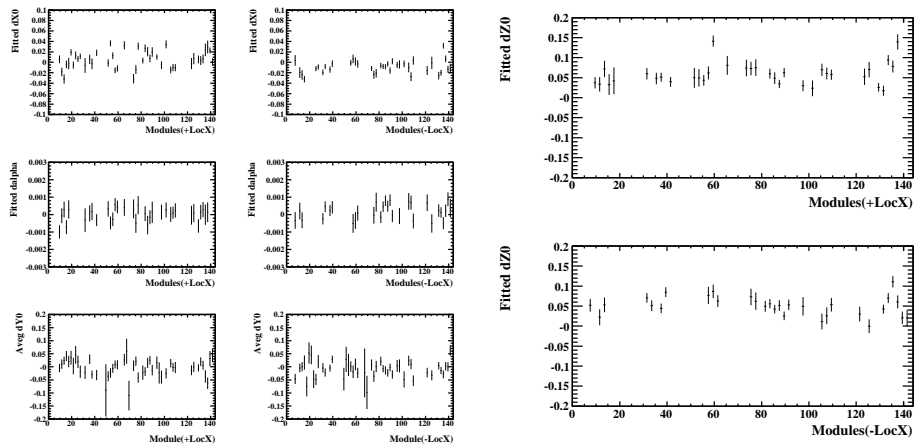


Figure 81: The relative alignment constants ( $dX_0$ ,  $dY_0$ ,  $d\alpha_0$  and  $dZ_0$ ) derived from the cosmic data as function of odd module in the overlap region with +LocX and -LocX.

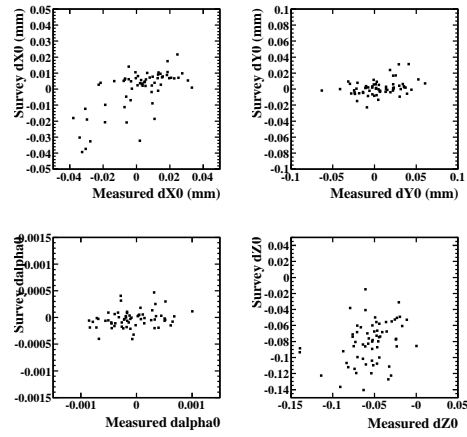


Figure 82: The scatter plot between the measured relative alignment and survey for neighboring modules.

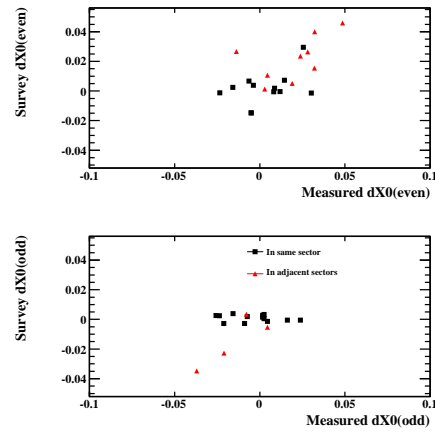


Figure 83: The scatter plot of relative alignment and survey between neighboring modules in the front disk or even modules (top) and in the back disk or odd modules (bottom). The back point is for modules in the same sector and the triangle point is for modules in different sectors.

## Alignment Results After Noise Removal

We have repeated the alignment studies using tracks that are neither from the noisy modules nor the hot pixels. As a result, the number of tracks considered in the study is reduced by approximately 26% and the resolution in LocX is improved from  $17.8\mu\text{m}$  to  $16.5\mu\text{m}$ , as shown in Figure 84. We have also checked the cluster resolution as function of cluster width in LocX. If we only consider clusters with cluster width=1, the resolution becomes  $14.8\pm 0.4\mu\text{m}$ , which is close to the intrinsic resolution, defined as  $50\mu\text{m}/\sqrt{12} = 14.4\mu\text{m}$ . Similarly, considering only clusters with width=2, a resolution of  $14.4\pm 0.3\mu\text{m}$  is obtained, as shown in Figure 85, which seems gain not much improvement as expected from charge sharing correction. One of the reasons could be residual misalignment, since alignment corrections have been applied only to overlaps, which have more than 50 hits.

The alignment constants obtained after noise removal are in a good agreement with the these reported in the previous section, as shown in Figure 86 (a). We also compared these alignment constants with an alternative alignment constants obtained from the same data that uses each pixel position in the cluster, instead of the cluster centroid. Details on that method can be found at <http://indico.cern.ch/conferenceDisplay.py?confId=16451>.

The correlations between these alignment constants are shown in Figure 86 (c) and (e). The comparisons of each set of alignment constants with the survey are also shown in Figure 86 (b), (d), and (f), respectively. It seems that alignment with noise removal improves agreement with survey.

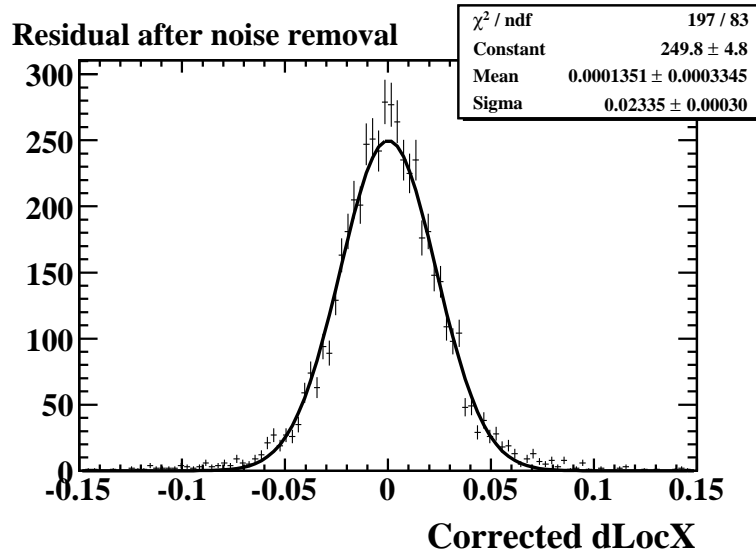


Figure 84: Residuals in LocX after noise removal and alignment correction.

## 8 Lesson learned and future improvements

In the previous sections there have been presented a wide spectrum set of studies that provides significant insight about what to expect when the full detector will be in operation.

First of all, from the noise measurements, it is possible to conclude that the most relevant noise source is *fixed pattern noise*, which in principle can be suppressed almost completely by masking, either on-line or off-line the noisy channels.

Almost the totality of noisy channels was detected as problematic during the module acceptance tests. Unfortunately, it is not possible, by the simple fact a pixels was *special* during these tests, to predict this specific pixel will be noisy. Therefore the number of *special* pixels can be taken as an upper limit to the inefficiencies, including both dead channels and channels masked because of the excessive noise rate. This number is few per mill of the total number of pixels.

Random noise, instead, is at a very low level and can be neglected for most application.

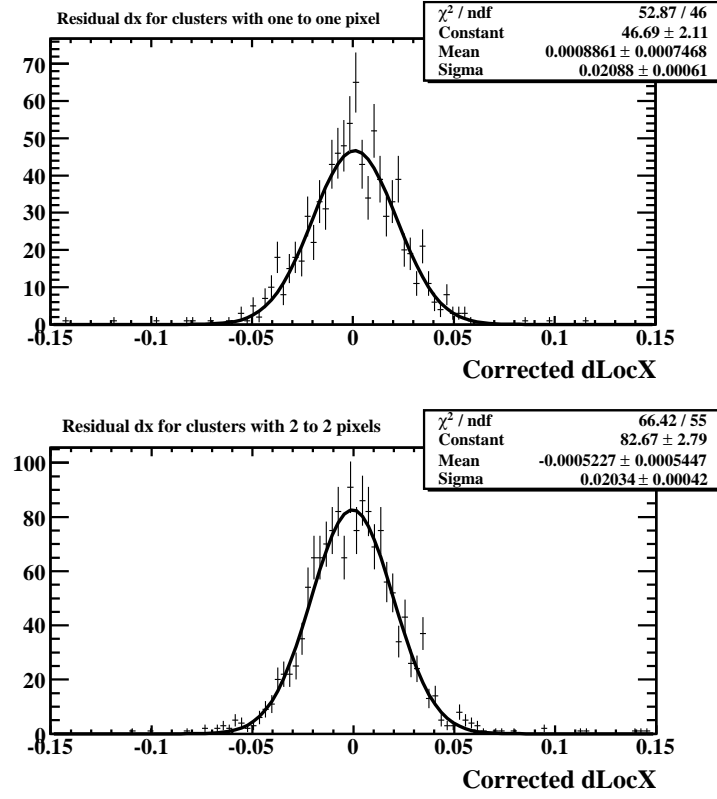


Figure 85: Residuals in LocX after noise removal and alignment correction for 1 pixel clusters(top) and 2 pixel clusters(bottom).

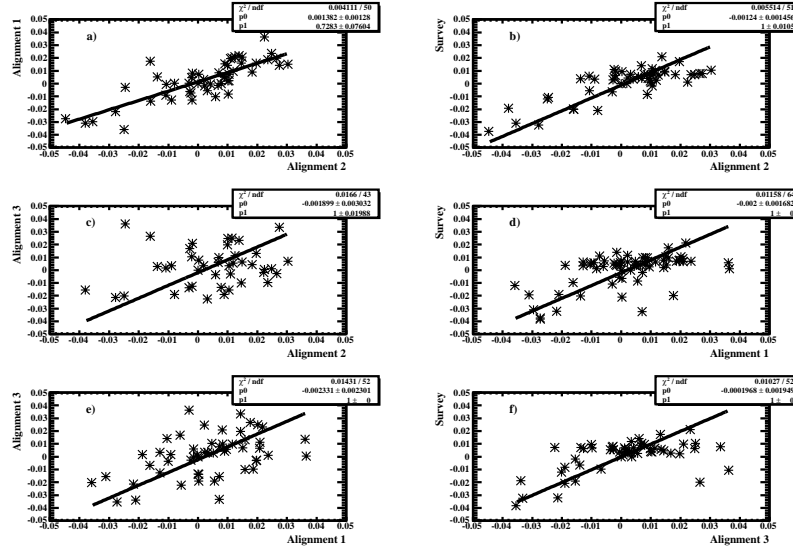


Figure 86: Scatter plots comparing the relative alignment constants between adjacent modules obtained from each study and the survey. Labels: Alignment 1 is at cluster level including noise; Alignment 2 is at cluster level after noise removal; Alignment 3 is at pixel level including noise.

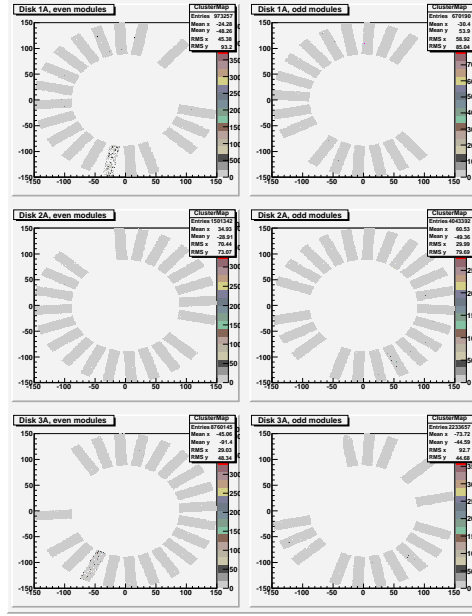


Figure 87: Cluster map for run 1129, before applying the special pixel production mask.

Digitization parameters have been taken from the characterization tests performed during module production. The simulation produced with these parameters has been compared with the collected data. This proved to be a good validation of the ATLAS pixel detector simulation and makes us confident that, extraction of calibration data on-site, from dedicated runs, will be a reliable source of updated information about the evolution of the detector operating conditions in the LHC running.

The tracking studies, especially the ones related to particles passing in the overlap regions between adjacent modules, have been very useful in spotting problems in our geometry description. In particular, different conventions in the detector description and Reconstruction software have been spotted and properly taken into account. Another observation was that a mismatch between the fabrication drawing and the actual detector assembly, initially observed in the sectors' survey, is confirmed by alignment data. The better agreement of alignment data with the survey than with the nominal drawings, show the survey is a reliable starting point.

This will be of much more relevance for the barrel part, since in that region the disagreement between the survey and nominal position is much worse, at the  $200\text{ }\mu\text{m}$  level.

Besides the analysis summarized above this run was a very useful opportunity to finalize many software updates needed for the detector commissioning, in particular a complete revision of the digitization, the implementation of a calibration database in COOL, which can be accessed both by simulation and reconstruction processes, and finally the insertion of the survey information to be used as initial alignment step. The technical aspects of this updates in the pixel software and description are described in an accompanying Computing System Commissioning note [19].

There are some additional studies interesting for the pixel offline analysis and calibration, which the impact of masking of the special pixels are discussed later.

These include the collection of DCS information, in order to estimate the amount of data that will be collected during normal data taking and smoothing parameters for the PVSS logging and transfer to COOL.

## 8.1 Impact of Masking of the Special Pixels

Figures 87 and 88 show the hitmaps for run 1129 before and after masking of the special pixels and the two noisiest modules. It is clear most of the spikes in the occupancy distribution disappear.

Noisy pixels give a constant background as function of the LVL1 accept, below the peak of hits in time with the trigger signals. The distribution of LVL1 accept before and after masking are shown

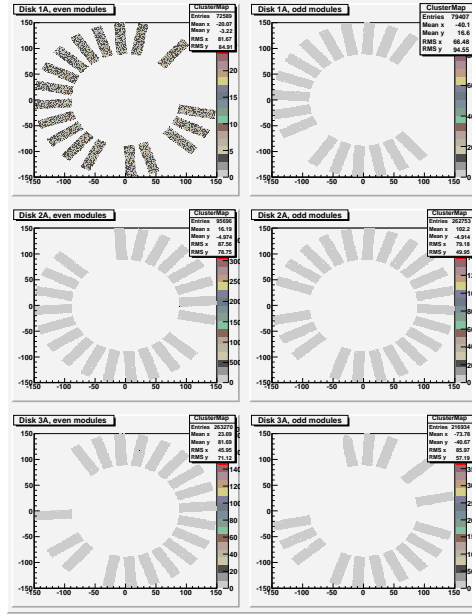


Figure 88: Cluster map for run 1129, after applying the special pixel production mask.

in Figures 89 and 90, respectively. From the value of this flat background, one derives that, after the pixels classified as unuseful are masked, the noise level drops significantly from an average occupancy of  $3 \times 10^{-7}$  to  $10^{-8}$ .

The remaining noise is still mostly concentrated on very few pixels.

Without masking the level of fake tracks in which noise hits are either linked together, or joined to few real hits, to form a new track, is significant, since associated noisy hits are visible in the bottom plot of Figure 89. The fake rate reduces to a negligible level after masking (bottom plot of Figure 90).

After removing the special pixels the total number of reconstructed tracks in this reduces from 26502 to 24836, but looking at the angular distribution of these tracks in Figure 91, it appear that the lost track are mostly localized excesses to the smooth distribution of track angles seen after noise removal.

Therefore it is possible to conclude that masking of the special pixels just removes fake tracks, generated by aligned noisy regions, but do not affect significantly the tracking efficiency.

After masking the special pixels, one can conclude that the rate of hits is 1.1 times the trigger rate, and the  $\geq 3$  hits tracks relative rate is 3.3%. Further more, we have made some comparison between the cosmic data and Monte Carlo when using the calibration from the database and noisy pixel masking, which are shown in Figure 92- 95 for track probability, the cluster width and its BCID, the number of pixel rows in the cluster, and the TOT for single, double and triple hits clusters, respectively. The data in blue (point) agree well with the Monte Carlo expectation in red (histogram).

## 9 Conclusion

This document summarizes the results of the offline analysis for the pixel endcapA system test cosmic data. The setup consists of one pixel endcap of three disks, for a total of 144 modules and 6.6 million channels, about the 8% of the full detector. The endcap is hung vertically and sandwiched between one scintillator at the top and a set of three scintillators at the bottom for trigger. It is completely equipped with services and managed by a initial production of the ATLAS DAQ system components with the goal of exercising the readout system, data taking and testing the offline reconstruction chain.

Runs with random trigger allow us to measure the noise rate. The observed noise occupancy per BCID readout is achieved to  $10^{-10}$  after removing the noisy pixels. Comparison with the detector characterization performed during the detector assembly shows that most of these noisy pixels were already flagged during the production test.

The tracking studies, especially the ones related to particles passing in the overlap regions between

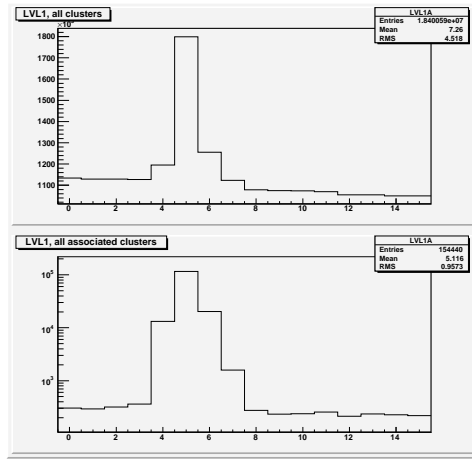


Figure 89: LVL1 distribution for pixel digits in run 1129, before applying the special pixel production mask. In the bottom plot only the digits associated to a track are shown, in logarithmic scale to show the small contribution of noise hits to the track reconstruction.

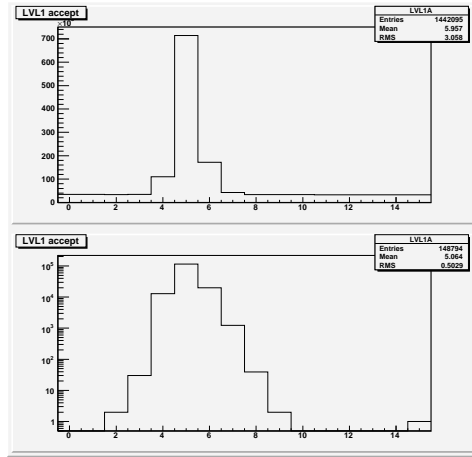


Figure 90: LVL1 distribution for pixel digits in run 1129, after applying the special pixel production mask. In the bottom plot only the digits associated to a track are shown, in logarithmic scale to show that there are essentially no contribution of noise hits to the track reconstruction.

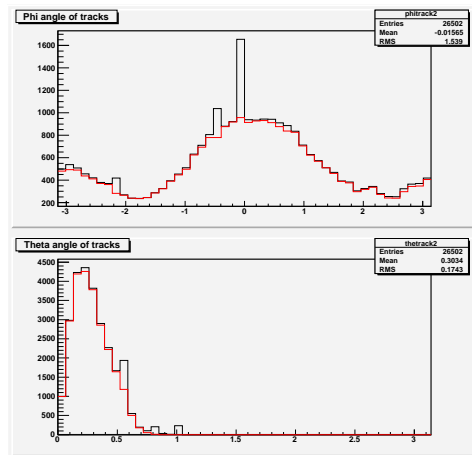


Figure 91: Top: azimuthal angle of reconstructed tracks. Bottom: polar angle of reconstructed tracks. Black lines are before, red lines are after the masking of special pixels.

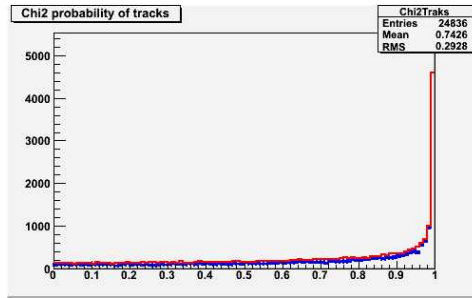


Figure 92: Comparison of track probability distribution between data in blue point and Monte Carlo in red histogram.

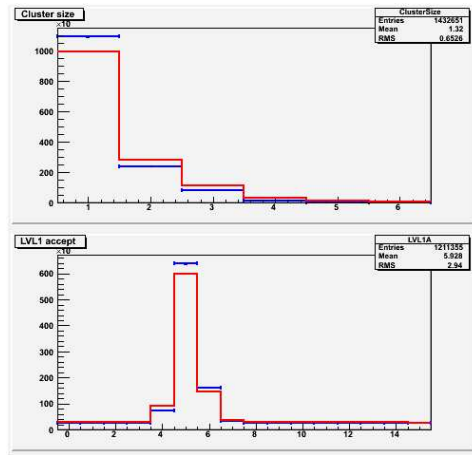


Figure 93: Comparison of the cluster width (top) and its BCID (bottom) between data in blue point and Monte Carlo in red histogram.

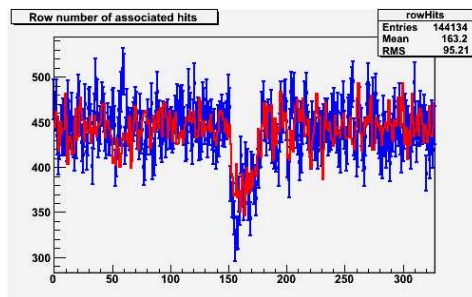


Figure 94: Comparison of the number of pixel rows in the cluster between data in blue point and Monte Carlo in red histogram.



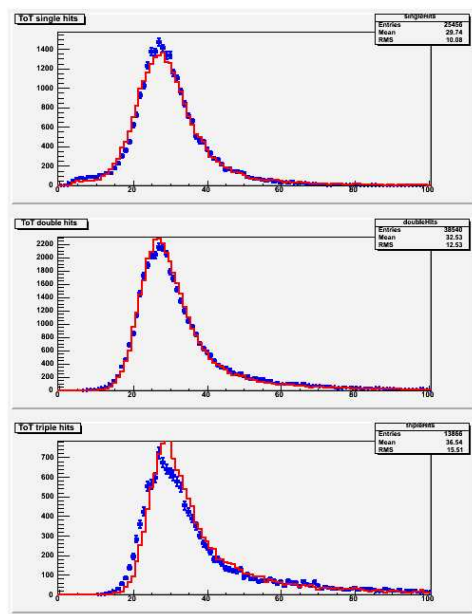


Figure 95: Comparison of the TOT distribution for single, double and triple clusters between data in blue point and Monte Carlo in red histogram.

adjacent modules, have been very useful in spotting problems in our geometry description and can be used for the relative alignment between the adjacent modules.

The characteristic of pixel clustering in the data are checked and agree well with Monte Carlo simulation. The pixel cluster efficiency are also measured to be close to 100% using the hits in the module overlap regions. When using the geometry taken from the detector survey, an initial resolution of  $21.2 \mu m$  is obtained. After a preliminary alignment this improves to  $17.8 \mu m$ . The difference with the  $15.8 \mu m$  expected from MC simulation are probably due to residual alignment uncertainties which are under investigation.

The experience gained in the SR1 running will be also extremely useful for the preparation of the cosmics running within the whole ATLAS setup in the pit and its analysis and understanding.

## References

- [1] M. Keil *et al.*, *Pixel Endcap A System Test*, in preparation.
- [2] M. Leyton *et al.* *Service Tests for the ATLAS Pixel Detector*, ATL-IP-QA-0026 (2007).
- [3] G. Alimonti *et al.*, *Analysis of testbeam data of ATLAS Pixel detector modules with a high intensity pion beam*, ATL-COM-INDET-2005-012, (2005).
- [4] M. Zdražil *et al.*, *Pixel EndCap A cosmic test documentation on A TLAS Twiki pages*, <https://twiki.cern.ch/twiki/bin/view/Atlas/PixelCosmic>.
- [5] M. Keil, P. Morettini *et al.*, *Pixel Detector System Test - ATLAS TWi ki pages*, <https://twiki.cern.ch/twiki/bin/view/Atlas/SystemTest>.
- [6] K. Einsweiler *et al.*, *ATLAS On-detector Electronics Architecture*, v ersion 3.0, Dec 9, 2003. Also see Kevin's presentation at LBNL Instrumentation Colloquium, April 13, 200 5, *The Atlas Pixel Detector*, p. 8-18 mainly.
- [7] K. Einsweiler *et al.*, *ATLAS On-detector Electronics Architecture*, v ersion 3.0, Dec 9, 2003. Also see Kevin's presentation at LBNL Instrumentation Colloquium, April 13, 200 5, *The Atlas Pixel Detector*, p. 8-18 mainly.

- [8] S. Golfarb and A. Schaffer *et al.*, *Definition of Off-line Readout Identifiers for the ATLAS Detector*, ATL-SOFT-2001-004, (2001).
- [9] SuDong, H. Gray *et al.*, *Pixel Scintillator Trigger Layout documentat ion - ATLAS TWiki pages*, <https://twiki.cern.ch/twiki/bin/view/Atlas/PixelScintillatorTriggerLayout>.
- [10] S. Eidelman *et al.*, *Review of Particle Physics*, Physics Letters \_f B 592, 1 (2004). See <http://pdg.lbl.gov> for Particle Listings and complete reviews, plus a direc tory of online HEP information.
- [11] A. di Simone *et al.*, *Cosmic simulation package documentation on ATLAS TWiki pages*, <https://twiki.cern.ch/twiki/bin/view/Atlas/CosmicSimulation>.
- [12] D. Costanzo, G. Gorfine, *PixelGeoModel package documentation on ATLAS TWik i pages*, <https://twiki.cern.ch/twiki/bin/view/Atlas/PixelGeoModel>.
- [13] M. Gallas and Simone Dell’Acqua *et al*, *GEANT4 ATLAS detector simulat ion applica-tions*, [http://atlas-computing.web.cern.ch/atlas-computing/packages/simulation/geant4/G\\_4Atlas-Apps/doc/index.html](http://atlas-computing.web.cern.ch/atlas-computing/packages/simulation/geant4/G_4Atlas-Apps/doc/index.html).
- [14] O. Oye *et al.*, *InDetCosmicSimAlgs simulation package documentation on ATLAS TWiki pages*, <https://twiki.cern.ch/twiki/bin/view/Atlas/InDetCosmicSimAlgs>.
- [15] M. Elsing, F. Tegenfeldt *et al.*, *ATLAS Pixel Detector digitization package on ATLAS TWiki pages*, <https://twiki.cern.ch/twiki/bin/view/Atlas/PixelDigitization>.
- [16] M. Zdražil *et al.*, *How to run simulation of pixel endcap A cosmic test*, <https://twiki.cern.ch/twiki/bin/view/Atlas/HowToRunPixelEndCapCCosmicSimulation>.
- [17] D. Dobos, J. Weingarten, private communication.
- [18] T. Cornelissen, *CTBtracking: track reconstruction for the testbeam and cosmics*, ATL-INDET-INT-2006-001 (2006).
- [19] *Pixel Software Commissioning*, in preparation
- [20] A. Andreazza, V. Kostyukhin, R. Madaras, *Pixel Survey*, ATL-IP-QC-0035 (in preparation).